Modular Arrangement of Synaptic and Intrinsic Homeostatic Plasticity within Visual Cortical Circuits

Wei Wen[1] and Gina G. Turrigiano[1,2]

[1]Department of Biology, Brandeis University, Waltham, MA 02453, USA

[2]Corresponding Author: turrigiano@brandeis.edu

Abstract

Neocortical circuits use synaptic and intrinsic forms of homeostatic plasticity to stabilize key features of network activity, but whether these different homeostatic mechanisms act redundantly, or can be independently recruited to stabilize different network features, is unknown. Here we used pharmacological and genetic perturbations both *in vitro* and *in vivo* to determine whether synaptic scaling and intrinsic homeostatic plasticity (IHP) are arranged and recruited in a hierarchical or modular manner within L2/3 pyramidal neurons in rodent V1. Surprisingly, although the expression of synaptic scaling and IHP was dependent on overlapping trafficking pathways, they could be independently recruited by manipulating spiking activity or NMDAR signaling, respectively. Further, we found that changes in visual experience that affect NMDAR activation but not mean firing selectively trigger IHP, without recruiting synaptic scaling. These findings support a modular model in which synaptic and intrinsic homeostatic plasticity respond to and stabilize distinct aspects of network activity.

Introduction

To reliably maintain computational power in the face of experience-dependent modifications, neocortical networks use homeostatic forms of plasticity to constrain important features of network activity (Turrigiano and Nelson, 2004). Defects in homeostatic plasticity contribute to pathological changes in network function by rendering circuits unable to compensate for perturbations arising during development or experience-dependent plasticity (Ellingford et al., 2021; Nelson and Valakh, 2015; Pratt et al., 2011; Radulescu et al., 2023; Ruggiero et al., 2021; Sohal and Rubenstein, 2019; Tatavarty et al., 2020). Many network features are under homeostatic control (Wen and Turrigiano, 2024), including mean firing rates (Hengen et al., 2016, 2013), sensory tuning curves (Noda et al., 2023; Rose et al., 2016), nearness to criticality (Ma et al., 2019), and the local correlation structure (Wu et al., 2020). There is also a great diversity in the underlying cellular homeostatic plasticity mechanisms, but whether particular cellular mechanisms operate in a modular manner to regulate specific network features is still unknown (Wen and Turrigiano, 2024). For example, while computational work suggests that circuits may independently recruit synaptic and intrinsic homeostatic plasticity to regulate distinct aspects of network function (Cannon and Miller, 2017, 2016; Ma et al., 2019; Wu et al., 2020), recent experimental work has instead suggested that they are functionally and mechanistically coupled and are thus recruited in tandem (Li et al., 2020). Here we set out to determine whether synaptic and intrinsic homeostatic plasticity are arranged in a coupled, hierarchical manner, or whether they sense different features of network activity and thus can be independently recruited.

Circuit homeostasis is realized through careful adjustments of excitatory and inhibitory elements at a number of network nodes. Cellular mechanisms of homeostatic plasticity include those that modulate excitatory synapses, inhibitory synapses, or intrinsic neuronal excitability (Debanne et al., 2019; Gainey and Feldman, 2017; Maffei and Turrigiano, 2008; Wen and Turrigiano, 2024). Among these, excitatory synaptic scaling and IHP have been observed in neocortical and hippocampal pyramidal neurons under a variety of experimental conditions (Breton and Stuart, 2009; Desai et al., 1999; Echegoyen et al., 2007; Greenhill et al., 2015; Karmarkar and Buonomano, 2006; Lambo and Turrigiano,

2013; Maffei and Turrigiano, 2008; Turrigiano et al., 1998; Wen and Turrigiano, 2021; Zbili et al., 2021), and can be triggered together by global activity manipulations and sensory deprivation (Lambo and Turrigiano, 2013; Wen and Turrigiano, 2021). In the primary visual cortex (V1), monocular deprivation during the classic visual system critical period initially suppresses firing rates and reduces pairwise network correlations (Hengen et al., 2013; Lambo and Turrigiano, 2013; Tatavarty et al., 2020); both of these network features are then homeostatically restored in parallel with the induction of synaptic scaling and IHP onto layer 2/3 (L2/3) pyramidal neurons (Hengen et al., 2016; Wu et al., 2020), and this homeostatic restoration is absent when these forms of plasticity are genetically ablated (Tatavarty et al., 2020; Wen and Turrigiano, 2021). Despite their co-induction during sensory deprivation, it is still unclear whether synaptic scaling and IHP respond to the same features of altered activity, or whether they might be differentially sensitive to changes in firing rates and network correlations. A major factor in this information gap is the lack of knowledge about the induction and expression mechanisms of IHP, and the degree to which these are shared with synaptic scaling. For example, many of the classic activity manipulations used to study homeostatic plasticity, including blockade of spiking with tetrodotoxin (TTX), disrupt multiple calcium-dependent signaling pathways in parallel (Wen and Turrigiano, 2024), and which of these is necessary to trigger IHP is unknown.

To determine whether synaptic scaling and IHP share induction and expression mechanisms, and are arranged hierarchically or in a modular manner within neocortical circuits, we first propose two models (Figures 1A and 1B). In the first hierarchical scenario, the expression of synaptic scaling occurs prior to and results in the induction of IHP (Li et al., 2020; Turrigiano, 2011; Figure 1A), implying that they should always be triggered by the same activity manipulations. Alternatively, synaptic scaling and IHP could be arranged in a modular manner in which they sense changes in distinct aspects of activity (Figure 1B); in this model it is still possible that the two forms of plasticity converge onto shared trafficking pathways (Figure 1B, upper panel).

To differentiate between these models, we perturbed different aspects of circuit activity *in vitro* and *in vivo*, and disrupted known trafficking pathways for synaptic scaling, to determine the co-dependence between synaptic scaling and IHP. We found that synaptic

scaling and IHP share many aspects of their expression mechanisms, including time course, sensitivity to tumor necrosis factor α (TNFα), and intracellular trafficking pathways. Surprisingly, we also found that synaptic scaling and IHP are independently induced by reduced spiking and diminished NMDA receptor (NMDAR) signaling, respectively. Further, we found that a light-driven increase in pairwise correlations in V1 downregulates intrinsic excitability through an NMDAR-dependent mechanism, without inducing synaptic scaling. These data establish that synaptic scaling and IHP are driven by different activity sensors and are thus sensitive to distinct changes in circuit activity, yet rely on similar molecular pathways for their expression. Our results are consistent with a modular model in which synaptic scaling and IHP can be independently recruited to serve distinct functions within V1 circuits.

Results

IHP follows a similar expression timeline as synaptic scaling *in vitro*

If synaptic scaling and IHP share either activity-sensors or induction pathways, then they should follow a similar timecourse and be sensitive to the same molecular manipulations. In cultured cortical and hippocampal neurons, both synaptic scaling and IHP can be robustly induced by chronic activity silencing using TTX (Desai et al., 1999; Lee et al., 2015; Stellwagen and Malenka, 2006; Turrigiano et al., 1998). Further, synaptic scaling can be induced *in vitro* within 4 hours (Ibata et al., 2008), and by 6 hours is robust and almost as large in magnitude as at 24 hours (Steinmetz and Turrigiano, 2010). To determine whether IHP follows a similar timecourse *in vitro*, we treated sister cultures with TTX for either 2 or 6 hours (Figure 1C), and measured the intrinsic excitability of pyramidal neurons by generating firing rate versus current (F-I) curves while blocking all synaptic transmissions (Figures 1D and 1E). There was already an upward shift in the F-I curve after 2 hours of TTX treatment compared to the non-treated (NT) condition (Figures 1E, 2h TTX vs. NT), although the difference in the areas under the F-I curve was not statistically significant (Figure 1F, 2h TTX vs. NT). Intrinsic excitability increased significantly after 6 hours of TTX treatment, (Figures 1E and 1F, 6h TTX vs. NT), and was associated with lower rheobase current (Figure 1G), shorter latency to the first spike (Figure 1H), a subtle but

significant narrowing of the first spike evoked at rheobase (Figure S1A, with no difference observed in the spike peak amplitude, Figure S1B), and higher neuronal input resistance (Figure S1C). In contrast, we did not observe any significant difference in action potential voltage threshold, spike frequency adaptation, or resting membrane potential (Figures S1D-S1F). Therefore, IHP expression also occurs rapidly in the first few hours of TTX treatment, closely following the timecourse of synaptic scaling.

A hallmark of TTX-induced synaptic scaling is its requirement for gene transcription (Gainey et al., 2015; Ibata et al., 2008; Schaukowitch et al., 2017; Steinmetz et al., 2016). To test whether IHP expression is also transcription-dependent, we co-treated cultures with actinomycin D (ActD) and TTX for 6 hours (Figures 1C and 1D). This prevented the normal TTX-induced change in the F-I curve (Figures 1E and 1F, ActD+TTX not different from NT), and there were no significant differences in other cellular and spiking properties (Figures 1G, 1H, S1A-S1F). Thus, like synaptic scaling, TTX-induced IHP depends on transcription in the early stage of its expression.

IHP expression requires TNFα signaling

The expression of synaptic scaling is dependent on the cytokine TNFα, which maintains synapses in a plastic state that allows them to respond to perturbations in firing (Barnes et al., 2017; Steinmetz and Turrigiano, 2010; Stellwagen and Malenka, 2006). Whether IHP is also dependent upon TNFα signaling is unknown. To test this, we began by assessing the dependence of IHP on TNFα in cultured cortical neurons, following the same experimental paradigm described in Steinmetz and Turrigiano, 2010 (Figure S2A). An important finding of this study was that pretreating neurons with a TNFα scavenger protein (Kaneko et al., 2008), sTNFR, for 24 hours completely blocked scaling up induced by 6 hours of TTX treatment. In contrast, co-treating neurons with sTNFR and TTX for 6 hours did not affect scaling up, indicating that a prolonged period of reduced TNFα signaling was necessary to block synaptic scaling. Intriguingly, the expression of TTX-induced IHP exhibited similar characteristics. While we still observed an increase in intrinsic excitability after 6 hours of TTX and sTNFR co-treatment (Figure S2B and S2C, sTNFR vs. Co), pretreating these neurons with sTNFR for 14-17 hours before adding TTX prevented this increase in excitability (Figure S2B and S2C, sTNFR vs. Pre). Analyses of spiking properties

revealed the same suite of changes as observed above (Figure S2D-S2F). These results demonstrate that – as for synaptic scaling – TNFα signaling plays a permissive role in TTX-induced IHP *in vitro*.

To determine whether this co-dependence on TNFα signaling is maintained in more mature *in vivo* circuits, we employed a previously validated activity suppression method, using the inhibitory DREADD hM4Di (Wen and Turrigiano, 2021; Figure 2A). We targeted hM4Di to excitatory neurons in V1 by delivering a Cre-dependent hM4Di construct packaged in an adeno-associated viral vector into the V1 of Emx1-Cre mice during the classical visual system critical period. After waiting 7-10 days for robust DREADD expression, we administered CNO to the animals via drinking water for 24 hours to suppress V1 network activity (Wen and Turrigiano, 2021). In addition, we inhibited TNFα signaling *in vivo* by administering Xpro1595 (Xpro), a small-molecule TNFα scavenger that can pass the blood brain barrier (Barnes et al., 2017). Based on our *in vitro* results, we pretreated animals with either Xpro or saline vehicle for 24 hours prior to the onset of the hM4Di silencing paradigm, followed by a second Xpro dose administered at the time animals were switched to CNO-containing drinking water (Figure 2A).

First, we confirmed that Xpro blocks synaptic scaling. We cut slices of V1 and recorded miniature excitatory postsynaptic currents (mEPSCs) from L2/3 pyramidal neurons, and compared mEPSC amplitude after activity suppression combined with either Xpro or vehicle administration (Figure 2B). Comparing hM4Di-positive and hM4Di-negative neurons in the presence of saline vehicle revealed a significant increase in the mean mEPSC amplitude (Figure 2C, Saline, DR+CNO vs. CNO) and a clear rightward shift of the cumulative distribution of the entire mEPSC event population (Figure 2D), indicating synaptic scaling had occurred in these hM4Di-poisitive neurons, as expected (Wen and Turrigiano, 2021). In contrast, the same comparison in animals that received Xpro revealed no significant increase in mEPSC amplitude (Figure 2C, Xpro, DR+CNO vs. CNO), and superimposable cumulative distributions (Figure 2E). There were no significant differences in either the mean mEPSC frequency or waveform kinetics across conditions (Figures S2G-S2I, Insets of Figures 2D and 2E). Thus, inhibiting TNFα signaling is sufficient to block DREADD-induced synaptic scaling up in V1 L2/3 pyramidal neurons.

Next, we repeated the hM4Di-mediated silencing paradigm but instead measured F-I curves from L2/3 pyramidal neurons, in the presence of synaptic blockers (Figure 2F). Consistent with our previous results (Wen and Turrigiano, 2021), we observed normal IHP expression in saline-treated animals, indicated by comparable increases in both the area under F-I curve and the slope of the linear region (Figures 2G and 2H, DR+CNO vs. CNO). Further analyses of spike waveforms and trains revealed that this increase in intrinsic excitability in saline-treated animals was accompanied by reductions in both the rheobase current and the latency to the first spike (Figures 3G and 3H, Saline) and an increase in input resistance (Figure 3F, Saline). No significant differences were observed in the spike width at half-maximum (Figure 3B, Saline), the action potential voltage threshold (Figures 3A and 3C, Saline), the afterhyperpolarization amplitude (Figure 3D, Saline), or in spike frequency adaptation (Figure 3I, Saline). Strikingly, IHP was absent in Xpro-treated littermates, with no significant difference in the intrinsic excitability of hM4Di-negative and -positive neurons (Figures 2I and 2J, DR+CNO vs. CNO). In line with these findings, neurons from both conditions in Xpro-treated animals had no significant difference in any measures of excitability (Figures 3B-3D, 3F-3I, Xpro). Interestingly, hM4Di-mediated activity suppression led to a small elevation of the spike peak amplitude in both saline- and Xpro-treated animals (Figure 3A, left; Figure 3E), suggesting that some more subtle effects of activity suppression are not dependent on TNFα signaling. In conclusion, TNFα signaling is required for maintaining the expression of both synaptic scaling and IHP in the intact visual cortex.

IHP is sensitive to molecular blockade of synaptic scaling expression *in vivo*

Our results so far establish that the induction of synaptic scaling and IHP share a number of features, suggesting that their induction might be interdependent. This could be explained by a hierarchical model, in which IHP is initiated by signaling pathways downstream of synaptic scaling expression (Figure 1A). This model predicts that blocking the expression of synaptic scaling will also abolish IHP.

To test this hypothesis, we manipulated a well-established molecular trafficking pathway for synaptic scaling to disrupt its expression. In neocortical and hippocampal pyramidal neurons, synaptic scaling relies on receptor trafficking interactions involving the

GluA2 subunit of AMPA receptors (AMPARs) (Gainey et al., 2015, 2009; Goold and Nicoll, 2010; Tan et al., 2015), and can be blocked in L2/3 pyramidal neurons by the expression of a GluA2 C-terminal tail (C-tail) fragment (Lambo and Turrigiano, 2013; Wen and Turrigiano, 2021). To determine whether the GluA2 C-tail also blocks IHP, we virally co-expressed hM4Di and the GluA2 C-tail in one hemisphere of V1, while only expressing hM4Di in the other hemisphere as a positive control (Wen and Turrigiano, 2021) (CT+ and CT-, Figures 4A and 4B). After administering CNO for 24 hours, we measured intrinsic excitability of L2/3 hM4Di-positive pyramidal neurons (Figures 4C and 4D). While the F-I curve from CT- neurons shifted upward and leftward as expected (Figures 4D and 4E, CT- vs. CT+), there was no significant change in intrinsic excitability of CT+ neurons (Figure 4E, CT+ vs. NT). As expected, CT- neurons had a lower rheobase current (Figure 4F), a shorter latency to the first spike (Figure 4G), and a slightly higher neuronal input resistance (Figure 4H) than CT+ neurons. In summary, these results show that DREADD-induced IHP expression, like synaptic scaling, is susceptible to blockade by the GluA2 C-tail fragment.

Synaptic Scaling and IHP can be Independently Induced by suppressing spikes or NMDAR signaling, respectively

The sensitivity of IHP to manipulations that affect AMPAR trafficking is consistent with two different models for how synaptic scaling and IHP interact. First, as illustrated in the hierarchical model, IHP induction could be triggered by effectors downstream of synaptic scaling induction, such as calcium influx through glutamate receptors added during scaling (Li et al., 2020; Figure 1A). In this scenario, IHP should not be inducible in the absence of synaptic scaling expression. Alternatively, synaptic scaling and IHP might be induced through separate signaling pathways, but rely on similar receptor/channel trafficking mechanisms during their expression (Figure 1B). To investigate these possibilities, we aimed to determine whether we could dissociate the induction of scaling and IHP by pharmacologically perturbing distinct aspects of circuit activity.

We started by treating cortical neurons from sister cultures either with TTX to block all spiking activity, or with an NMDAR antagonist, APV, to block NMDAR-mediated transmissions (Figure 5A). Importantly, TTX, which reduces but does not completely eliminate NMDAR activity (Sutton et al., 2006; Watt et al., 2000), robustly induces scaling

(Turrigiano et al., 1998), whereas APV, which blocks NMDAR signaling but has little effect on spiking activity, does not induce scaling (Leslie et al., 2001; Turrigiano et al., 1998). To determine whether IHP is also insensitive to NMDAR blockade, we measured the intrinsic excitability of neurons treated with TTX, APV, or both (Figures 5B and 5C). Surprisingly, we found that APV treatment alone induced IHP with a comparable magnitude to that induced by TTX treatment (Figures 5C-5E, APV: 227% [area] and 148% [slope] of NT, TTX: 194% [area] and 167% [slope] of NT). Further, co-application of TTX and APV did not lead to a larger shift of the F-I curve (Figures 5C-5E, TTX+APV, 200% [area] and 154% [slope] of NT), indicating that these two manipulations are not additive. Last, the IHP expression observed under all three conditions was accompanied by similar changes in rheobase, spike latency, and input resistance (Figures 4F, S3F, and S3G), suggesting that the expression mechanisms are similar. As in previous datasets we found no major difference in other cellular properties including action potential voltage threshold, spike width at half-maximum, spike peak amplitude, spike adaptation index, and resting membrane potential (Figures S3A-S3E, S3H). Importantly, we verified that APV does not induce synaptic scaling (Figure 7E). Together these data show that IHP can be induced independently of synaptic scaling expression, and suggest that it is driven by reduced intracellular calcium influx through NMDARs.

It has been suggested that a form of intrinsic homeostatic plasticity featuring action potential broadening can be triggered by calcium influx through calcium-permeable GluA1-containing AMPARs targeted to the synapses during chronic TTX silencing (Li et al., 2020). If activation of calcium-permeable AMPARs is critical for intrinsic plasticity, then blocking their activity should prevent IHP from occurring. We therefore treated cultured neurons with philanthotoxin (PhTX), a selective antagonist for calcium-permeable AMPARs, and assayed TTX-induced IHP (Figure 5G). Unlike TTX or APV, chronic PhTX treatment did not induce IHP on its own (Figures 5G and 5H, PhTX vs. NT). Furthermore, addition of PhTX did not prevent TTX-induced IHP (Figures 5G and 5H, PhTX+TTX vs. TTX), and there was no broadening of action potentials in any condition (Figures 5I and 5J), consistent with our previous datasets (Figures S1A, S3A and S3C). These results demonstrate that action potential broadening is not a feature of TTX- or APV-induced IHP in cortical pyramidal

neurons measured either *in vitro* (Figure 5C) or *ex vivo* (Figure 2G), and activation of calcium-permeable AMPARs does not contribute to this form of IHP.

We next wished to test whether suppressing NMDAR activity alone *in vivo* would also induce IHP. We used CPP, an NMDAR antagonist that blocks NMDAR-dependent Hebbian plasticity with little impact on visual function (Sato and Stryker, 2008; Torrado Pacheco et al., 2021; Toyoizumi et al., 2014). We used the same paradigm developed for the Xpro experiments, but instead of Xpro, we injected animals with CPP (Figure 6A). Following DREADD-mediated induction of IHP, we recorded F-I curves from L2/3 pyramidal neurons in the V1 of animals treated with either CPP or saline (Figures 6A-6C). Analyses of the F-I curves from these two groups of animals revealed two clear effects (Figures 6C and 6D). First, neurons from CPP-treated animals exhibited higher intrinsic excitability than those from saline-treated littermates at baseline (Figure 6D, CPP-CNO vs. Saline-CNO). Second, despite the normal IHP expression in hM4Di-positive neurons from saline-treated animals (Figure 6D, Saline, DR+CNO vs. CNO), CPP induced no additional increase in intrinsic excitability in the hM4Di-positive neurons, indicating a lack of additivity (Figure 6D, CPP, DR+CNO vs. CNO, 95% of CNO). As for DREADD-mediated IHP, this CCP-induced increase in intrinsic excitability was associated with a lower rheobase, a shorter latency to the first spike, and a higher input resistance (Figures 6E-6G). These results show that CPP-mediated suppression of NMDAR activity induces IHP in the intact visual cortex, and likely occludes further DREADD-mediated IHP.

Together these *in vitro* and *ex vivo* data provide strong evidence that IHP and synaptic scaling can be induced independently, and are sensitive to distinct aspects of neuronal activity: IHP by reduced NMDAR signaling and synaptic scaling through reduced spike-mediated calcium influx (Ibata et al., 2008). These data argue against the hierarchical model (Figure 1A) and instead favor a model in which they are induced in parallel (Figure 1B).

IHP, but not synaptic scaling, can be suppressed through allosteric modulation of NMDAR signaling

We found that reducing NMDAR activity pharmacologically induces IHP but not scaling, arguing for differential sensitivities to NMDAR signaling. An important prediction of this finding is that TTX should not be able to induce IHP under conditions where NMDAR activity is enhanced. To test this prediction, we used a positive allosteric modulator of NMDAR, GLYX-13 (GLYX) (Moskal et al., 2005), and examined its effect on TTX-induced IHP in cultured cortical neurons (Figure 7A). Strikingly, co-application of TTX and GLYX completely abolished IHP (Figures 7B and 7C, TTX+GLYX vs. NT), indicating that, when spiking is blocked, enhancing NMDAR activity is sufficient to prevent the induction of IHP. Examination of other cellular properties also revealed no difference between TTX +GLYX and the NT group (Figures S4A-S4F).

If NMDAR signaling is unimportant for the induction of synaptic scaling, then GLYX should have no impact on the ability of TTX to induce scaling up. To test this, we repeated the GLYX treatment and examined synaptic scaling by recording mEPSCs (Figure 7D). As expected, mEPSC amplitudes of neurons co-treated with GLYX and TTX were still scaled up when compared to the NT group (Figure 7E, TTX+GLYX vs. NT), showing a similar magnitude of increase as the neurons treated with TTX alone (Figure 7E, TTX vs. NT). We then generated cumulative distributions of mEPSC amplitude from these conditions, and found that TTX and TTX+GLYX populations were statistically indistinguishable, but both were significantly different from the NT population (Figure 7F). GLYX had no effect on mEPSC frequency, waveform kinetics, or passive neuronal properties (Figures S4G-S4I). Thus, synaptic scaling will occur as long as spiking activity is suppressed. Finally, we verified that APV alone was not able to induce scaling up (Figure 7E, APV vs. NT), consistent with previous work (Turrigiano et al., 1998). These data show that neither reducing nor enhancing NMDAR signaling influences synaptic scaling.

Synaptic Scaling and IHP can be independently recruited during normal sensory experience

Taken together, the results described above show that IHP is induced via changes in NMDAR signaling, while synaptic scaling induction relies on altered spiking activity. An

important implication of this finding is that it should be possible to independently recruit IHP without inducing synaptic scaling *in vivo* during experience-dependent manipulations that change NMDAR activation but leave mean firing rates unaffected. We showed previously that - while mean firing rates of V1 cortical neurons are stable across light and dark conditions - their pairwise correlations are significantly higher in the light than in the dark (Torrado Pacheco et al., 2019). Given that correlated pre- and postsynaptic firing is a strong trigger for calcium influx through postsynaptic NMDARs (Malenka and Bear, 2004), we predicted that L2/3 pyramidal neurons would have higher intrinsic excitability in the dark (when correlations and thus NMDAR signaling is low) than in the light (when correlations and thus NMDAR signaling is high), while synaptic scaling should be unaffected.

To test this idea, we first verified that pairwise correlations in V1 are higher in the light than in the dark, by re-analyzing chronic electrophysiological recordings of single-unit activity from V1 of freely behaving animals (Torrado Pacheco et al., 2021). To follow the change in correlation across light and dark, we picked a 24-hour period spanning 12 hours of light and 12 hours of dark, and computed the pairwise correlation coefficients for all pairs of regular-spiking units (putative pyramidal neurons) in consecutive 30-minute bins. Plotting the mean normalized pairwise correlation against time clearly illustrated a higher average correlation in the light period, with a rapid drop in correlation at the transition to dark (Figure 8A). Comparing the correlation matrices from an ensemble of continuously recorded neurons within one animal across the light and dark periods revealed that the same pairwise correlations exist in both conditions, but are stronger in the light (Figure 8B). Comparing the normalized correlation for each pair of neurons demonstrates that the majority of these neuronal pairs exhibited higher correlation in the light (Figure 8C, 21/25 pairs). In contrast, across multiple V1 datasets mean firing rates remain stable across light and dark periods (Hengen et al., 2016, 2013; Torrado Pacheco et al., 2019).

If the light-driven increase in correlations enhances postsynaptic NMDAR activation, this should trigger a slow reduction in intrinsic excitability that should be robustly expressed after 6 hours (e.g. Figures 1E and 1F). To test this, we cut acute slices from littermates at two timepoints: right before the end of the 12-hour dark period (Figure 8D,

left, ZT 0h), and 6 hours into the subsequent light period (Figure 8D, left, ZT 6h). We then examined intrinsic excitability of V1 L2/3 pyramidal neurons at these two timepoints by recording F-I curves (Figures 8E and 8F). Indeed, intrinsic excitability was lower after animals spent 6 hours in the light than at the end of the dark period (Figures 8F and 8G, Light 6h vs. Dark 0h). To verify that this reduction in excitability was driven by light rather than circadian time, we kept a third group of littermates in the dark for an additional 6 hours before sacrificing them for recordings (Figure 8D, right, ZT 6h). Remarkably, when animals were kept in prolonged darkness there was no reduction in intrinsic excitability (Figures 8F and 8G, Dark 6h vs. Dark 0h), indicating that IHP is driven by light exposure rather than circadian entrainment. Further analyses of spike trains revealed that the light-driven reduction in intrinsic excitability was accompanied by increases in the rheobase (Figure S5J, left three groups) and latency to the first spike (Figure S5K, left three groups), and a reduction in the neuronal input resistance (Figure S5L, left three groups), just as for DREADDs- and TTX-induced IHP. In sum, these results show that perturbations associated with light-driven changes in pairwise correlations trigger IHP in freely behaving animals.

Since the mean firing rates of V1 neurons are stable across light and dark, and we have shown that synaptic scaling is insensitive to changes in NMDAR signaling, mEPSC amplitude should be stable across the same light/dark conditions. To test this, we recorded mEPSCs from V1 L2/3 pyramidal neurons from acute slices obtained at the same timepoints (Figure S5A). As expected, there was no difference in either the mean mEPSC amplitudes or the cumulative amplitude distributions across all three timepoints (Figures S5B and S5C). Furthermore, light/dark exposure had no impact on mEPSC kinetics (Figure S5C, inset; Figures S5D and S5E). On the other hand, we noticed a small increase in mEPSC frequency in the light condition that was absent in the prolonged dark condition (Figures S5F and S5G); this may reflect additional forms of plasticity set in motion by changes in correlation or other light-driven effects.

If light-driven correlations reduce intrinsic excitability by enhancing NMDAR activation, then this should be blocked or reduced by acutely suppressing NMDAR activity *in vivo* during light exposure. To test this, we administered either CPP or saline to the animals at the dark-to-light transition (Figure 8H), and again measured intrinsic

excitability. We first verified that acute CPP administration had only minor effects on activity, by quantifying cFos expression in V1 (Figure S5H), and found no significant impact on the number of cFos-positive neurons relative to saline (Figure S5I, CPP vs. Saline). Next, we administered saline or CPP to littermates just before the dark/light transition (Figure 8H, ZT 0h), and exposed them to light for 6 hours before sacrificing them for slice electrophysiology (Figure 8H, ZT 6h). Consistent with our prediction, neurons from animals treated with CPP had higher intrinsic excitability than saline-treated animals, indicating that CPP-mediated NMDAR inhibition was sufficient to partially reverse the light-driven changes in intrinsic excitability (Figures 8I-8K, CPP vs. Saline). This change in excitability was accompanied by the usual cellular changes associated with IHP (Figures S5J-S5L, right two groups). These data demonstrate that the light-driven reduction in intrinsic excitability is realized through downstream signaling involving NMDARs. More broadly, our results make clear that synaptic scaling and IHP in L2/3 pyramidal neurons are driven by different activity-sensors, and are thus sensitive to distinct aspects of network activity.

Discussion

Several distinct forms of homeostatic plasticity have been documented within the same neocortical circuits, but the degree to which they act redundantly, or can be independently recruited to stabilize different aspects of network activity, is unclear. Here we used both *in vitro* and *ex vivo* electrophysiology paired with pharmacological and genetic manipulations to determine whether two such mechanisms, synaptic scaling and IHP, are arranged hierarchically or in parallel in neocortical pyramidal neurons. We found that synaptic scaling and IHP rely on many of the same molecular pathways for their expression, yet are sensitive to and activated by different features of network activity: while synaptic scaling is induced by changes in mean firing rates, IHP is instead induced by changes in NMDAR activation. Further, we demonstrated that sensory experience that alters NMDAR signaling but leaves mean firing rate unaffected selectively recruits IHP but not synaptic scaling. Our results show that synaptic scaling and IHP are triggered by different activity sensors, supporting a model where individual homeostatic plasticity mechanisms act in a modular manner to regulate distinct network features.

Despite a growing computational literature arguing that distinct cellular homeostatic mechanisms could be used to independently control important circuit features (Cannon and Miller, 2017, 2016; Ma et al., 2019; Wu et al., 2020), we have only a rudimentary understanding of when and how different forms of homeostatic plasticity are engaged within biological circuits. Like other forms of plasticity, homeostatic plasticity can be roughly split into induction and expression pathways (Figures 1A and 1B). During induction neurons detect a perturbation away from some activity set-point to initiate plasticity, while expression requires changes in ion channel surface abundance and distribution to generate a compensatory response. There is convincing evidence that synaptic scaling is induced when mean firing rate deviates from a firing rate set point (Goold and Nicoll, 2010; Hengen et al., 2016; Ibata et al., 2008; Turrigiano et al., 1998), and since synaptic scaling and IHP are often induced in parallel (Desai et al., 1999; Lambo and Turrigiano, 2013; Turrigiano et al., 1998; Wen and Turrigiano, 2021), it was reasonable to assume they are initiated by the same activity sensor during induction. One study compatible with this view proposed that a hierarchy exists between the induction of synaptic and intrinsic plasticity (Li et al., 2020). In this scenario (Figure 1A), synaptic scaling occurs prior to IHP, enhances calcium influx through calcium-permeable AMPARs, and this then initiates a form of intrinsic plasticity that involves spike broadening. In contrast, our results clearly demonstrate that IHP can be induced independently of scaling; blocking NMDAR-mediated signaling *in vitro* or *in vivo* induces IHP but not synaptic scaling, IHP induction can be suppressed during spiking blockade by enhancing NMDAR signaling even though synaptic scaling still occurs, and IHP is not affected by block of calcium-permeable AMPARs. While it is possible that spike broadening occurs under some conditions via different induction rules, we found no evidence for spike broadening in any of our *in vitro* or *in vivo* manipulations that dramatically modulate firing rates, here (Figures 3B, 5I, S1A, S3C, S4D) or in previous work from our lab and others (Ritzau-Jost et al., 2021; Trojanowski and Turrigiano, 2021; Wen and Turrigiano, 2021). Our data showing that scaling and IHP can each be induced independently of the other rule out a hierarchical model, and instead establish that scaling and IHP are sensitive to distinct aspects of network activity (Figure 1B).

These results are surprising in light of many observations that scaling and IHP can be disrupted by the same molecular manipulations. For example, both are driven by changes in intracellular calcium (Goold and Nicoll, 2010; Ibata et al., 2008; Li et al., 2020), are modulated by CaMKIV signaling (Joseph and Turrigiano, 2017, but see Trojanowski and Turrigiano, 2021), and are sensitive to loss of the multidomain scaffolding protein Shank3 (Tatavarty et al., 2020; Wen and Turrigiano, 2021). Our findings strongly suggest that the calcium sources that trigger these two forms of plasticity are different; while scaling is more sensitive to spike-driven calcium influx (Ibata et al., 2008), we show here that IHP is likely dependent on calcium influx through NMDAR, consistent with a previous study (Lee et al., 2015). Taken together, this suggests that scaling and IHP are triggered via different calcium sources, but converge onto overlapping molecular pathways downstream of calcium influx during plasticity expression. This dependence on distinct calcium sources is an efficient way to allow synaptic scaling and IHP to sense different aspects of network activity, and thus serve distinct compensatory roles within the circuit.

A variety of molecular players have been implicated in the expression of scaling (Fernandes and Carvalho, 2016; Turrigiano, 2012), but very little is known about the mechanisms underlying IHP. We show here that IHP expression shares many features and dependencies with synaptic scaling. Both require protein synthesis, are sensitive to TNFα signaling, involve trafficking mechanisms that are disrupted by expression of a GluA2 C-terminal fragment, and unfold with a similar time course. The endpoint of both synaptic scaling and IHP is the regulation of the surface abundance and distribution of the ion channels that determine postsynaptic strength (AMPAR) or intrinsic excitability (voltage-gated ion channels; Debanne et al., 2019; Desai et al., 1999; Lee et al., 2015). It thus makes sense that both forms of plasticity utilize transcription- and translation-dependent protein synthesis (Schanzenbächer et al., 2018, 2016; Schaukowitch et al., 2017; Valakh et al., 2023), and might share common protein trafficking and recycling/degradation pathways (Dörrbaum et al., 2020; Fernandes and Carvalho, 2016; Gainey et al., 2015; Steinmetz et al., 2016; Tan et al., 2015). Synaptic scaling relies on C-terminal interactions between the GluA2 subunit of the AMPAR and synaptic proteins such as GRIP1 (Gainey et al., 2015; Tan et al., 2015), and disruption of GluA2 trafficking via expression of a GluA2 C-tail fragment

blocks scaling both *in vitro* and *in vivo* (Gainey et al., 2009; Lambo and Turrigiano, 2013; Wen and Turrigiano, 2021). Given that IHP does not require the prior induction of synaptic scaling, we were surprised to find that this same manipulation can also prevent IHP. One possible explanation is that this C-terminal fragment interferes with other more general ion channel trafficking pathways, such as the crucial protein interactions with cell-adhesion and cytoskeletal molecules during the membrane localization of voltage-gated ion channels (Ferron et al., 2021; Leterrier et al., 2010), or the recycling endosomal pathways that shuttle membrane-bound proteins between different membrane compartments (Nakatsu and Ohno, 2003; Robinson and Bonifacino, 2001; Steinmetz et al., 2016).

If synaptic scaling and IHP are functionally distinct, which circuit features do they stabilize, respectively? Many features of neocortical network activity are known to be under homeostatic control, including mean firing rates (Hengen et al., 2016, 2013), sensory tuning curves (Noda et al., 2023; Rose et al., 2016), the nearness of the network to criticality (Ma et al., 2019), and the local correlation structures (Wu et al., 2020). The induction of synaptic scaling and IHP is correlated with the homeostasis recovery of mean firing rates and pairwise correlation structure during prolonged sensory deprivation (Hengen et al., 2016, 2013; Lambo and Turrigiano, 2013). Here we find that the induction of scaling is driven by changes in firing, while IHP is driven by changes in NMDAR signaling, which is modulated by correlated firing reflected in pairwise network correlations. Importantly, we found that light exposure, which drives an increase in the magnitude of existing pairwise correlations but has little impact on mean firing rates (Torrado Pacheco et al., 2019; Figure 8A), results in a sufficient change in NMDAR-mediated signaling to trigger IHP, without triggering scaling. These findings show that neocortical circuits can selectively recruit IHP in response to changes in NMDAR signaling incurred through long-lasting changes in correlated firing, and potentially any other cellular or network changes that enhance NMDAR activation. Despite sensing correlations, it is unlikely that IHP feeds back to directly exert homeostatic control over pairwise correlation structure, as IHP develops gradually while the change in correlations across light and dark is abrupt and quite stable after the shift has occurred. Alternatively, because IHP is likely to modulate dendritic excitability (Fan et al., 2005; Gasselin et al., 2015; Wierenga et al., 2005), it may be that IHP induction

directly regulates NMDAR activation by affecting the ease with which synaptic inputs can depolarize the dendrite to remove the voltage-dependent magnesium block. In this scenario IHP would sense and homeostatically regulate NMDAR activation itself. Alternatively, IHP might regulates other circuit features such as the variance in the timing of spikes (coefficient of variation [CV] of interspike intervals; Cannon and Miller, 2016; Hengen et al., 2013). Indeed, we have consistently observed that IHP changes the slope of F-I curves rather than the firing threshold (Figures 2G, 3C, 5E, S3B), which is predicted to magnify the impact of both excitatory and inhibitory inputs on spike probability, thus magnifying spike variance; IHP induction during monocular deprivation would then restore CV, as observed experimentally (Hengen et al., 2013). Either of these scenarios would leave synaptic scaling free to homeostatically regulate mean firing rate and/or pairwise correlation structure.

It has long been proposed that different forms of cellular homeostatic plasticity are instrumental in the homeostatic maintenance of distinct features of network activity, yet how homeostatic plasticity is arranged within neural circuits to achieve this was unclear. Taken together our results demonstrate that synaptic and intrinsic forms of homeostatic plasticity, even when expressed in the same cell type, sense distinct aspects of activity perturbations and thus can be independently recruited *in vivo*. These mechanistic differences between synaptic and intrinsic plasticity induction allows them to act either in concert or independently, and to regulate distinct aspects of network function. Together, our findings support the idea that key network features are independently constrained by different cellular homeostatic mechanisms to ensure that circuits can remain functional in the face of a wide range of perturbations.

Acknowledgments

We thank members of the Turrigiano lab for constructive discussions and Lirong Wang for the help in neuronal culture maintenance. This work was supported by funding from R35NS111562 (to G.G.T.).

Author Contributions

Conceptualization, W.W. and G.G.T.; Methodology, W.W. and G.G.T.; Investigation, W.W.; Writing- Original Draft, W.W.; Writing- Review & Editing, W.W. and G.G.T.; Visualization, W.W.; Funding Acquisition, G.G.T.

Declaration of Interests

The authors declare no competing interests.

Materials and Methods

Key Resource Table

REAGENT or RESOURCE	SOURCE	IDENTIFIER
Antibodies		
Rat monoclonal anti-mCherry	Invitrogen	Cat#: M11217
Rabbit polyclonal anti-GFP	Invitrogen	Cat#: A11122
Guinea pig polyclonal anti-NeuN	Synaptic systems	Cat#: 266004
Rabbit monoclonal anti-cFos	Cell signaling	Cat#: 2250
Goat anti-rabbit Alexa Fluor 488	Invitrogen	Cat#: A11070
Goat anti-rabbit Alexa Fluor 594	Invitrogen	Cat#: A11037
Goat anti-rat Alexa Fluro 594	Invitrogen	Cat#: A11007
Goat anti-guinea pig Alexa Fluro 488	Invitrogen	Cat#: A11073
Anti-streptavidin Alexa Fluro 488	Invitrogen	Cat#: S11223
Anti-streptavidin Alexa Fluro 594	Invitrogen	Cat#: S11227
Bacterial and virus strains		
AAV9-hSyn-DIO-hM4D(Gi)-mCherry	Addgene	Cat#: 44362
AAV-CMV-GluA2(CT)-GFP	Lambo and Turrigiano, 2013	N/A
Chemicals, peptides, and recombinant proteins		
Tetrodotoxin (TTX)	Abcam (discontinued); Alomone	Cat#: 120055 (Abcam); T-550 (Alomone)
DL-APV	Tocris	Cat#: 0105
Picrotoxin	Tocris	Cat#: 1128
Actinomycin D (ActD)	Millipore Sigma	Cat#: A9415
6,7-dinitroquinoxaline-2,3-dione (DNQX)	Millipore Sigma	Cat#: D0540
Philanthotoxin-7,4	Hello Bio	Cat#: HB0499
CNO dihydrochloride	Hello Bio	Cat#: HB6149
Xpro1595	INmune Bio	N/A
(RS)-CPP	Tocris	Cat#: 0173
Recombinant Mouse sTNF RI/TNFRSF1A Protein (sTNFR)	R&D systems	425-R1-050
GLYX 13	Tocris	Cat#: 3406
Deposited data		
Raw and analyzed data	This paper	
Chronic recording data	Torrado Pacheco et al., 2021	

Experimental models: Cell lines		
Primary neuronal culture from Crl:LE Long-Evans Rat	Charles River Laboratory	RRID: RGD_2308852
Experimental models: Organisms/strains		
Mouse: C57BL/6J, wild-type (WT),	Jackson Labs	RRID: IMSR_JAX:000664
Mouse: C57BL/6J, Emx1-cre	Jackson Labs	B6.129S2-Emx1tm1(cre)Krj/J RRID: IMSR_JAX:017688
Software and algorithms		
MATLAB	Mathworks	https://www.mathworks.com
Image J	National Institute of Health	https://imagej.nih.gov/ij/
Illustrator	Adobe	https://www.adobe.com/products/illustrator.html
Photoshop	Adobe	https://www.adobe.com/products/photoshop.html

Data and code availability

All data generated in this study are included in this article and can be accessed at figshare: https://figshare.com/s/46391f11318beff5b6bb. All scripts used for analysis have been deposited at the following URL: https://github.com/turrigianoCodeSpace/WeiWenManuscript2024.

Experimental Model and Subject Details

All experimental procedures performed in this study strictly followed the protocols approved by the Brandeis Animal Care and Use Committee (IACUC) and Institutional Biosafety Committee (IBC), which complied with Guide for the Care and Use of Laboratory Animals from the National Institute of Health. Animals were housed on a 12:12 light/dark cycle with *ad libitum* access to food and water (except when experiments dictated otherwise, see below). Pups were weaned between postnatal days (P) 19-21 and housed with at least one littermate (except when experiments required single-housing). For all experiments, both males and females were used; no sex-dependent difference was observed and therefore results were not separated by sex. For *in vitro* primary neuronal cultures, newborn pups between P0-3 from timed-pregnant Long-Evans rats were used for dissociation. C57BL/6J mice were used for all *ex vivo* slice physiology experiments, which were performed between P24-32 to capture the classic rodent visual system critical period. The number of animals used for each experiment are given in the corresponding figure legend.

Primary neuronal culture

Primary neuronal cultures were dissociated from the visual cortex of newborn rat pups (P0-3) as previously described (Tatavarty et al., 2020; Wu et al., 2022). Briefly, pups were anesthetized with isofluorane and decapitated, and the visual cortex was removed and incubated at 37 °C with an enzyme solution containing 25 U/mL papain, 1 mM L-cystein, and 0.5 mM EDTA. The tissue was then rinsed and suspended with trypsin before being centrifuged at low speed for 5 minutes. The

pellet was resuspended with neuronal medium supplemented with NS21 (Pratt et al., 2003) and plated onto 35 mm glass-bottomed dishes pre-seeded with glial feeders. Cultures were incubated in a 5% CO_2 incubator at 37 °C until being used for experiments, and were fed every 3-4 days by replacing 1 mL of old medium with fresh medium.

Drug treatment/administration

Cultured neurons

Primary neuronal cultures were treated with specific pharmacological agents between 9 and 14 days in vitro (DIV), usually up to 24 hours before being used for electrophysiology. Key drugs used in this study are listed in the Key Resource Table; all drugs were dissolved in Milli-Q water except for ActD, which was dissolved in 5% DMSO/PBS (working DMSO concentration 0.08%). The concentrations of drugs are as follows: TTX, 4 μM; DL-APV, 100 μM; Philanthotoxin, 10 μM; sTNFR, 2 μg/mL; GLYX-13, 1 μM; ActD, 50 μM.

Animals

For DREADD activation, CNO dihydrochloride (CNO) was delivered to the animals via drinking water as described previously (Wen and Turrigiano, 2021). Briefly, CNO was dissolved in tap water to 0.05 mg/mL with 10 mM saccharine chloride added. Animals were given saccharine-only water with the same concentration for a day before being switched to a CNO-containing one. They were sacrificed for experiments after 24 hours of CNO administration unless indicated otherwise.

For other drug administrations including Xpro1595 and CPP, the drug was dissolved in 0.9% sterile saline to the desired concentration (Xpro1595, 1 mg/mL; CPP, 1.5 mg/mL). Appropriate amounts of the drug solution were then delivered to the animals via subcutaneous injection to reach desired dosages (Xpro1595, 10 mg/kg; CPP, 15 mg/kg).

Virus Injection surgery

Virus injection surgeries were performed between P14-19 on a stereotaxic apparatus while animals were anesthetized with ketamine/xylazine/acepromazine cocktail (KXA). The monocular region of the primary visual cortex (V1m) was targeted unilaterally using stereotaxic coordinates (Allen Brain Atlas) that were proportionally adjusted according to the age-dependent bregma-lambda distance difference. Unless noted otherwise, 200-300 nL of virus were delivered into the targeted area via a micropipette. Surgerized animals were allowed to recover in their home cages for a week before slice physiology experiments.

Transcardial perfusion

Animals were anesthetized with a triple dose of KXA used for virus injection surgery. They were then transported to a fume hood, and the heart was exposed, and a needle was inserted into the left ventricle. The right atrium was then cut open, and 1x PBS was perfused through the circulatory system using a peristaltic pump for 5 minutes. The PBS was switched to 4% paraformaldehyde (PFA) when the liver color turned into light-brown, and the perfusion continued for about 5 minutes. The brain was then removed and incubated in 4% PFA with shaking at 4 °C overnight.

Immunocytochemistry

For acute slices, following slice physiology recordings, slices were post-fixed in 4% PFA overnight and transferred to 1x PBS for storage before staining. For all other immunostaining experiments, the fixed brain was mounted on a Leica VT1000S vibratome (Leica Biosystems, Buffalo Grove IL), and V1 was sectioned into 60 µm slices. Slices were washed in 1x PBS for at least 30 min (6 x 5 min) before being incubated in a blocking solution (0.1% Triton X-100, 0.05% NaN_3, and 1% BSA in 1x PBS) for 1 hour. Blocked slices were then incubated in the same blocking solution with primary antibodies added (1:1000) at 4 °C for 24 hours. The following day, slices were washed for 30 min in PBS and then incubated in a solution (0.05% NaN_3 and 1% BSA in 1x PBS) containing secondary antibodies (1:500). Acute slices were incubated at 4 °C overnight, all other slices were incubated at room temperature for 3 hours. Finally, slices were washed for another 30 min before mounted in Fluoromount G mounting medium (Southern Biotech, AL) and images were obtained using Zeiss LSM880 confocal microscope (Zeiss, Oberkochen Germany).

Ex vivo acute slice preparation

Animals were anesthetized with isoflurane. After toe-pinch check, the animal was decapitated and coronal slices (300 µm) containing V1m from both hemispheres were obtained using a Leica VT1000S vibratome. Slices were first transferred to an oxygenated chamber filled with choline solution (in mM: 110 Choline-Cl, 25 $NaHCO_3$, 11.6 Na-Ascorbate, 7 $MgCl_2$, 3.1 Na-Pyruvate, 2.5 KCl, 1.25NaH_2PO_4, and 0.5 $CaCl_2$, osmolarity adjusted to 310 mOsm with dextrose, pH 7.4) for recovery, and then transferred back to oxygenated standard artificial cerebrospinal fluid (ACSF, in mM: 126 NaCl, 25 $NaHCO_3$, 3 KCl, 2 $CaCl_2$, 2 $MgSO_4$, 1 NaH_2PO_4, 0.5 Na-Ascorbate, osmolarity adjusted to 310 mOsm with dextrose, pH 7.4) and incubated for 40 min. Slices were used for electrophysiology 1-5 hours post slicing.

Electrophysiology

Experimental setup

For culture electrophysiology, 35 mm glass-bottom dishes with primary neuronal culture were rinsed with ACSF (in mM: 126 NaCl, 25 $NaHCO_3$, 3 KCl, 2 $CaCl_2$, 2 $MgSO_4$, 1 NaH_2PO_4, 0.5 Na-Ascorbate, osmolarity adjusted to 320 mOsm with dextrose, pH 7.4) and placed on an Olympus IX70 upright fluorescence microscope. Neurons were superfused in oxygenated ACSF at 32° C throughout the experiment. Pyramidal neurons were visually identified by their morphology under a 20x objective, and then approached and patched under a 40x objective. Borosilicate glass pipettes with resistance between 3-7 MΩ were filled with $KMeSO_4$-based internal solution (in mM: 120 $KMeSO_4$, 10 KCl, 10 HEPES, 0.5 EGTA, 2 $MgSO_4$, 10 Na-Phosphocreatine, 3 K_2-ATP, and 0.3 Na-GTP, osmolarity adjusted to 310 mOsm with dextrose, pH adjusted to 7.4 with KOH).

For slice electrophysiology, coronal slices containing V1 were placed on an Olympus BX51WI upright epifluorescence microscope equipped with infrared-DIC optics. V1m was identified as previously described (Wen and Turrigiano, 2021). Pyramidal neurons were visually targeted for whole-cell recordings using a 40x water-immersion objective; visual identification was based on the teardrop shaped somata and the presence of an apical dendrite, and morphology was confirmed

post hoc from biocytin fill reconstructions. Neurons expressing exogeneous proteins were identified by the fluorescent marker embedded in the corresponding constructs. Borosilicate glass pipettes with resistance between 4 to 6 MΩ were filled with K^+ Gluconate-based internal solution (in mM: 100 K-gluconate, 10 KCl, 10 HEPES, 5.37 Biocytin, 0.5 EGTA, 10 Na-Phosphocreatine, 4 Mg-ATP, and 0.3 Na-GTP, osmolarity adjusted to 295 mOsm with sucrose, pH adjusted to 7.4 with KOH). All recordings were performed in slices that were superfused in oxygenated standard ACSF at 34 °C.

All electrophysiological recordings were performed using a Multiclamp 700B amplifier with a CV-7B headstage (Molecular Devices, Sunnyvale CA). Data were passed through a 6 kHz Bessel low-pass filter and acquired at 10 kHz using a National Instruments Data Acquisition Board (DAQ, National Instruments, Woburn, MA) and an open-source MATLAB-based software WaveSurfer (HHMI Janelia, Ashburn VA).

mEPSC recordings

For spontaneous mEPSC recordings, cultured neurons or slices were superfused with standard ASCF containing a drug cocktail of tetrodotoxin (TTX, 0.1 μM), D-2-amino-5-phosphonovalerate (APV, 50 μM), and picrotoxin (25 μM) to isolate mEPSCs. Pyramidal neurons were targeted and held at -70 mV in whole-cell voltage clamp, and series resistance was not compensated. Each neuron was recorded for 3-5 minutes in a series of 30s segments, and a 500 ms 5 mV hyperpolarizing voltage step was applied at the beginning of each segment so that passive properties could be monitored throughout the recording. Neurons were excluded if series resistance was > 20 MΩ, input resistance was < 100 MΩ (70 MΩ for culture), membrane potential was > -55 mV (-50 mV for culture), or these properties changed by > 15%.

Intrinsic excitability measurements

For intrinsic excitability measurements, cultured neurons or slices were superfused with standard ACSF containing APV (50 μM), picrotoxin (25 μM), and DNQX (25 μM) to block synaptic currents. Pyramidal neurons were held in current clamp with a small DC current injection to maintain the resting membrane potential at -60 mV (culture) or -70 mV (slice). Pipette capacitance was then neutralized, and bridge balance was compensated. Frequency versus current (F-I) curves were obtained by delivering a series of 0.5 s (culture) or 1 s (slice) long current injections in amplitude increments of 25 pA (culture) or 20 pA (slice). To monitor passive neuronal properties (except the resting membrane potential) throughout the recording, a 500ms 50 pA hyperpolarizing current step was applied before each current injection step. To monitor resting membrane potential changes, neurons were held in current clamp without any current injection and recorded for 1 minute before and after F-I curve measurements. To measure rheobase currents for cultured neurons, the rheobase was first estimated by locating the current step that had evoked the first spike during the F-I curve measurement, then 5 0.5 s long current steps starting from the previous lower current step and with amplitude increments of 5 pA were injected until a spike was evoked. Neurons that did not meet the criteria listed above for mEPSC recordings were excluded; in addition, neurons were excluded if the deviation of baseline membrane potential from their corresponding holding potentials was > 5% or the voltage firing threshold was >-25 mV.

Quantification and statistical analysis

All data obtained in this study were analyzed using in-house scripts written in MATLAB except the immunohistochemistry images, which were analyzed using Image J. Results illustrated via box plots are reported as median with 25th and 75th percentiles, with individual data points shown on the side; results shown in other types of plot are reported as described in the corresponding figure legends. Effect sizes are reported as a percentage of the group of interest (indicated in either the main text or the legend); samples sizes (the number of animals used for each experiment and the number of neurons collected for each condition), statistical tests performed, and *p* values are given in either the corresponding results section or the figure legends.

mEPSC recordings

Spontaneous mEPSC events were automatically detected using an in-house MATLAB script (modified from Miska et al., 2018). Briefly, the script filters the raw recording trace and then slides a mEPSC event-shaped template to find regions that fit the detection criteria (Cary and Turrigiano, 2021). Detected putative mEPSC events were then passed through multiple quality control modules to exclude the ones that were determined to be false-positive. Mean amplitude and frequency were first calculated for each 30 s of recording, which were then averaged to give the mean value for each neuron. Rise time and decay time constants were calculated from the waveform average traces for each neuron. Rise time is defined as the time for the current to increase from 10% to 90% of the peak amplitude. For mEPSC recordings, decay time constant (τ) is derived from a first-order exponential fit of the decay phase. To generate the cumulative distribution and the average waveform for each condition, 100 events were randomly selected from each neuron and pooled.

Intrinsic excitability recordings

Raw recordings obtained during the intrinsic excitability measurement were used for analysis without any filtering. For traces with depolarizing current injections, spikes were automatically detected using an in-house MATLAB script mainly based on the maximum dV/dt (> 20 V/s) and the peak amplitude (> 0 mV). Definitions of single spike or spike train properties analyzed in this study were primarily adapted from the electrophysiology technical white paper published by Allen Institute (https://celltypes.brain-map.org).

Briefly, for a given current step with a spike train, instantaneous firing rate (IFR) is defined as the mean reciprocal of the first two inter-spike intervals; mean instantaneous firing rate (mean IFR) is defined as the mean reciprocal of all inter-spike intervals; latency is defined as the time difference between the current step onset and the first spike; spike frequency adaptation is defined as the rate at which firings speeds up or slows down during the current step, and calculated as the mean normalized difference between two consecutive inter-spike intervals (higher values indicate more adaptation). For a given neuron, rheobase is defined as the smallest depolarizing current injection that has evoked one or more spikes.

For single spike properties, the first spike evoked at the rheobase is used for analysis unless noted otherwise. Spike threshold is defined as the membrane potential where dV/dt exceeds 5% of the maximum dV/dt during the depolarizing phase (Wen and Turrigiano, 2021). Spike width at half-

maximum is defined as the full width at half maximum of the spike height. Afterhyperpolarization (AHP) amplitude is defined as the difference between the minimum membrane potential reached after a spike and the mean membrane potential between the current step onset and the spike threshold (normalized to the spike height of the same cell).

Immunohistochemistry images

To quantify the number of cFos-positive neurons in mouse V1, images obtained from post-staining slices (against cFos and NeuN) were first background-subtracted and thresholded against the mean intensity of the NeuN signal from 3 negative control slices imaged in the same session (secondary antibodies only). A region of interest (ROI) of 250x200 μm was then manually selected from V1, and cFos signal was automatically background-subtracted. Cell somas were outlined in the NeuN channel, and cFos signals were measured in each identified cell soma. Cells that showed non-zero mean intensity values in the cFos channel were considered cFos-positive neurons. For each animal, 10-12 ROIs that spanned V1 were selected, and the percentage of cFos-positive neurons was reported for each ROI.

Pairwise correlation analysis

The data set used for correlation analysis was obtained from chronic multielectrode recordings from the control hemispheres of V1m of freely behaving Long-Evans rats, between the ages of P21 and P36, obtained in a previous study (Torrado Pacheco et al., 2021). Only animals that had at least two regular spiking units (RSUs) were included in the analysis. In total, 17 regular spiking units (RSUs) from 5 animals were used. Pairwise correlation coefficients of V1 neurons were calculated as previously described (Torrado Pacheco et al., 2019; Wu et al., 2020). Briefly, the spike timestamps for each neuron were divided into 100 ms bins, and the spike count was computed for each bin, which generated a spike count vector for each neuron. For each animal, the Pearson correlation coefficient r of spike counts was computed for a neuronal pair in 30-minute episodes with a 5-minute sliding window, producing 139 values for each pair in a 12-hour session. These values were then normalized to the mean correlation value of a selected baseline window (see Figure 8A legend). Example correlation matrices were generated from 5 neurons from 1 animal.

Statistical analysis

All data sets were first subjected to a normality test (Shapiro-Wilk test). For normally distributed data, an unpaired two-sample t test was used for pairwise comparison, and a one-way ANOVA followed by Tukey post hoc correction was used for multiple comparisons (no. of groups > 2). For other data, a Mann-Whitney U test was used for pairwise comparison, and a Kruskal-Wallis test followed by Tukey post hoc correction was used for multiple comparison. For distribution comparisons, a two-sample Kolmogorov-Smirnov test was used. Results were considered significant if $p < 0.05$.

References

Barnes, S.J., Franzoni, E., Jacobsen, R.I., Erdelyi, F., Szabo, G., Clopath, C., Keller, G.B., Keck, T., 2017. Deprivation-Induced Homeostatic Spine Scaling In Vivo Is Localized to Dendritic Branches that Have Undergone Recent Spine Loss. Neuron *96*, 871-882.e5. https://doi.org/10.1016/j.neuron.2017.09.052

Breton, J.D., Stuart, G.J., 2009. Loss of sensory input increases the intrinsic excitability of layer 5 pyramidal neurons in rat barrel cortex. J. Physiol. *587*, 5107–5119. https://doi.org/10.1113/jphysiol.2009.180943

Cannon, J., Miller, P., 2017. Stable Control of Firing Rate Mean and Variance by Dual Homeostatic Mechanisms. J. Math. Neurosci. *7*, 1. https://doi.org/10.1186/s13408-017-0043-7

Cannon, J., Miller, P., 2016. Synaptic and intrinsic homeostasis cooperate to optimize single neuron response properties and tune integrator circuits. J. Neurophysiol. *116*, 2004–2022. https://doi.org/10.1152/jn.00253.2016

Cary, B.A., and Turrigiano, G.G. (2021). Stability of neocortical synapses across sleep and wake states during the critical period in rats. eLife *10*, e66304. https://doi.org/10.7554/eLife.66304.

Debanne, D., Inglebert, Y., Russier, M., 2019. Plasticity of intrinsic neuronal excitability. Curr. Opin. Neurobiol. *54*, 73–82. https://doi.org/10.1016/j.conb.2018.09.001

Desai, N.S., Nelson, S.B., Turrigiano, G.G., 1999. Activity-dependent regulation of excitability in rat visual cortical neurons. Neurocomputing *26–27*, 101–106. https://doi.org/10.1016/S0925-2312(99)00004-1

Dörrbaum, A.R., Alvarez-Castelao, B., Nassim-Assir, B., Langer, J.D., Schuman, E.M., 2020. Proteome dynamics during homeostatic scaling in cultured neurons. eLife *9*, e52939. https://doi.org/10.7554/eLife.52939

Echegoyen, J., Neu, A., Graber, K.D., Soltesz, I., 2007. Homeostatic Plasticity Studied Using In Vivo Hippocampal Activity-Blockade: Synaptic Scaling, Intrinsic Plasticity and Age-Dependence. PLOS ONE *2*, e700. https://doi.org/10.1371/journal.pone.0000700

Ellingford, R.A., Panasiuk, M.J., De Meritens, E.R., Shaunak, R., Naybour, L., Browne, L., Basson, M.A., Andreae, L.C., 2021. Cell-type-specific synaptic imbalance and disrupted homeostatic plasticity in cortical circuits of ASD-associated Chd8 haploinsufficient mice. Mol. Psychiatry. *26*, 3614–3624. https://doi.org/10.1038/s41380-021-01070-9

Fan, Y., Fricker, D., Brager, D.H., Chen, X., Lu, H.-C., Chitwood, R.A., Johnston, D., 2005. Activity-dependent decrease of excitability in rat hippocampal neurons through increases in Ih. Nat. Neurosci. *8*, 1542–1551. https://doi.org/10.1038/nn1568

Fernandes, D., Carvalho, A.L., 2016. Mechanisms of homeostatic plasticity in the excitatory synapse. J. Neurochem. *139*, 973–996. https://doi.org/10.1111/jnc.13687

Ferron, L., Koshti, S., Zamponi, G.W., 2021. The life cycle of voltage-gated Ca2+ channels in neurons: an update on the trafficking of neuronal calcium channels. Neuronal Signal. *5*. https://doi.org/10.1042/NS20200095

Gainey, M.A., Feldman, D.E., 2017. Multiple shared mechanisms for homeostatic plasticity in rodent somatosensory and visual cortex. Philos. Trans. R. Soc. Lond. B. Biol. Sci. *372*, 20160157. https://doi.org/10.1098/rstb.2016.0157

Gainey, M.A., Hurvitz-Wolff, J.R., Lambo, M.E., Turrigiano, G.G., 2009. Synaptic Scaling Requires the GluR2 Subunit of the AMPA Receptor. J. Neurosci. *29*, 6479–6489. https://doi.org/10.1523/JNEUROSCI.3753-08.2009

Gainey, M.A., Tatavarty, V., Nahmani, M., Lin, H., Turrigiano, G.G., 2015. Activity-dependent synaptic GRIP1 accumulation drives synaptic scaling up in response to action potential blockade. PNAS *112*, E3590-3599. https://doi.org/10.1073/pnas.1510754112

Gasselin, C., Inglebert, Y., Debanne, D., 2015. Homeostatic regulation of h-conductance controls intrinsic excitability and stabilizes the threshold for synaptic modification in CA1 neurons. J. Physiol. *593*, 4855–4869. https://doi.org/10.1113/JP271369

Goold, C.P., Nicoll, R.A., 2010. Single-Cell Optogenetic Excitation Drives Homeostatic Synaptic Depression. Neuron *68*, 512–528. https://doi.org/10.1016/j.neuron.2010.09.020

Greenhill, S.D., Ranson, A., Fox, K., 2015. Hebbian and Homeostatic Plasticity Mechanisms in Regular Spiking and Intrinsic Bursting Cells of Cortical Layer 5. Neuron *88*, 539–552. https://doi.org/10.1016/j.neuron.2015.09.025

Hengen, K.B., Lambo, M.E., Van Hooser, S.D., Katz, D.B., Turrigiano, G.G., 2013. Firing Rate Homeostasis in Visual Cortex of Freely Behaving Rodents. Neuron *80*, 335–342. https://doi.org/10.1016/j.neuron.2013.08.038

Hengen, K.B., Torrado Pacheco, A., McGregor, J.N., Van Hooser, S.D., Turrigiano, G.G., 2016. Neuronal Firing Rate Homeostasis Is Inhibited by Sleep and Promoted by Wake. Cell *165*, 180–191. https://doi.org/10.1016/j.cell.2016.01.046

Ibata, K., Sun, Q., Turrigiano, G.G., 2008. Rapid synaptic scaling induced by changes in postsynaptic firing. Neuron *57*, 819–826. https://doi.org/10.1016/j.neuron.2008.02.031

Joseph, A., Turrigiano, G.G., 2017. All for One But Not One for All: Excitatory Synaptic Scaling and Intrinsic Excitability Are Coregulated by CaMKIV, Whereas Inhibitory Synaptic Scaling Is Under Independent Control. J. Neurosci. *37*, 6778–6785. https://doi.org/10.1523/JNEUROSCI.0618-17.2017

Kaneko, M., Stellwagen, D., Malenka, R.C., Stryker, M.P., 2008. Tumor Necrosis Factor-α Mediates One Component of Competitive, Experience-Dependent Plasticity in Developing Visual Cortex. Neuron *58*, 673–680. https://doi.org/10.1016/j.neuron.2008.04.023

Karmarkar, U.R., Buonomano, D.V., 2006. Different forms of homeostatic plasticity are engaged with distinct temporal profiles. Eur. J. Neurosci. *23*, 1575–1584. https://doi.org/10.1111/j.1460-9568.2006.04692.x

Lambo, M.E., Turrigiano, G.G., 2013. Synaptic and Intrinsic Homeostatic Mechanisms Cooperate to Increase L2/3 Pyramidal Neuron Excitability during a Late Phase of Critical Period Plasticity. J. Neurosci. *33*, 8810–8819. https://doi.org/10.1523/JNEUROSCI.4502-12.2013

Lee, K.Y., Royston, S.E., Vest, M.O., Ley, D.J., Lee, S., Bolton, E.C., Chung, H.J., 2015. N-methyl-D-aspartate receptors mediate activity-dependent down-regulation of potassium channel genes during the expression of homeostatic intrinsic plasticity. Mol. Brain *8*, 4. https://doi.org/10.1186/s13041-015-0094-1

Leslie, K.R., Nelson, S.B., Turrigiano, G.G., 2001. Postsynaptic Depolarization Scales Quantal Amplitude in Cortical Pyramidal Neurons. J. Neurosci. *21*, RC170–RC170. https://doi.org/10.1523/JNEUROSCI.21-19-j0005.2001

Leterrier, C., Brachet, A., Fache, M.-P., Dargent, B., 2010. Voltage-gated sodium channel organization in neurons: Protein interactions and trafficking pathways. Neurosci. Lett. *486*, 92–100. https://doi.org/10.1016/j.neulet.2010.08.079

Li, B., Suutari, B.S., Sun, S.D., Luo, Z., Wei, C., Chenouard, N., Mandelberg, N.J., Zhang, G., Wamsley, B., Tian, G., Sanchez, S., You, S., Huang, L., Neubert, T.A., Fishell, G., Tsien, R.W., 2020. Neuronal Inactivity Co-opts LTP Machinery to Drive Potassium Channel Splicing and Homeostatic Spike Widening. Cell *181*, 1547-1565.e15. https://doi.org/10.1016/j.cell.2020.05.013

Ma, Z., Turrigiano, G.G., Wessel, R., Hengen, K.B., 2019. Cortical Circuit Dynamics Are Homeostatically Tuned to Criticality In Vivo. Neuron *104*, 655-664.e4. https://doi.org/10.1016/j.neuron.2019.08.031

Maffei, A., Turrigiano, G.G., 2008. Multiple Modes of Network Homeostasis in Visual Cortical Layer 2/3. J. Neurosci. *28*, 4377–4384. https://doi.org/10.1523/JNEUROSCI.5298-07.2008

Miska, N.J., Richter, L.M., Cary, B.A., Gjorgjieva, J., and Turrigiano, G.G. (2018). Sensory experience inversely regulates feedforward and feedback excitation-inhibition ratio in rodent visual cortex. eLife *7*, e38846. https://doi.org/10.7554/eLife.38846.

Malenka, R.C., Bear, M.F., 2004. LTP and LTD: An Embarrassment of Riches. Neuron *44*, 5–21. https://doi.org/10.1016/j.neuron.2004.09.012

Moskal, J.R., Kuo, A.G., Weiss, C., Wood, P.L., O'Connor Hanson, A., Kelso, S., Harris, R.B., Disterhoft, J.F., 2005. GLYX-13: A monoclonal antibody-derived peptide that acts as an *N*-methyl-d-aspartate receptor modulator. Neuropharmacol. *49*, 1077–1087. https://doi.org/10.1016/j.neuropharm.2005.06.006

Nakatsu, F., Ohno, H., 2003. Adaptor Protein Complexes as the Key Regulators of Protein Sorting in the Post-Golgi Network. Cell Struct. Funct. *28*, 419–429. https://doi.org/10.1247/csf.28.419

Nelson, S.B., Valakh, V., 2015. Excitatory/Inhibitory Balance and Circuit Homeostasis in Autism Spectrum Disorders. Neuron *87*, 684–698. https://doi.org/10.1016/j.neuron.2015.07.033

Noda, T., Kienle, E., Eppler, J.-B., Aschauer, D.F., Kaschube, M., Loewenstein, Y., Rumpel, S., 2023. Homeostasis of a representational map in the neocortex. Preprint at BioRxiv. https://doi.org/10.1101/2023.06.13.544358

Pratt, K.G., Watt, A.J., Griffith, L.C., Nelson, S.B., and Turrigiano, G.G. (2003). Activity-Dependent Remodeling of Presynaptic Inputs by Postsynaptic Expression of Activated CaMKII. Neuron *39*, 269–281. https://doi.org/10.1016/S0896-6273(03)00422-7.

Pratt, K.G., Zimmerman, E.C., Cook, D.G., Sullivan, J.M., 2011. Presenilin 1 regulates homeostatic synaptic scaling through Akt signaling. Nat Neurosci 14, 1112–1114. https://doi.org/10.1038/nn.2893

Radulescu, C.I., Doostdar, N., Zabouri, N., Melgosa-Ecenarro, L., Wang, X., Sadeh, S., Pavlidi, P., Airey, J., Kopanitsa, M., Clopath, C., Barnes, S.J., 2023. Age-related dysregulation of homeostatic control in neuronal microcircuits. Nat. Neurosci. 1–13. https://doi.org/10.1038/s41593-023-01451-z

Ritzau-Jost, A., Tsintsadze, T., Krueger, M., Ader, J., Bechmann, I., Eilers, J., Barbour, B., Smith, S.M., Hallermann, S., 2021. Large, Stable Spikes Exhibit Differential Broadening in Excitatory and Inhibitory Neocortical Boutons. Cell Rep. *34*, 108612. https://doi.org/10.1016/j.celrep.2020.108612

Robinson, M.S., Bonifacino, J.S., 2001. Adaptor-related proteins. Curr. Opin. Cell Biol. *13*, 444–453. https://doi.org/10.1016/S0955-0674(00)00235-0

Rose, T., Jaepel, J., Hübener, M., Bonhoeffer, T., 2016. Cell-specific restoration of stimulus preference after monocular deprivation in the visual cortex. Science *352*, 1319–1322. https://doi.org/10.1126/science.aad3358

Ruggiero, A., Katsenelson, M., Slutsky, I., 2021. Mitochondria: new players in homeostatic regulation of firing rate set points. Trends. Neurosci. *44*, 605–618. https://doi.org/10.1016/j.tins.2021.03.002

Sato, M., Stryker, M.P., 2008. Distinctive Features of Adult Ocular Dominance Plasticity. J. Neurosci. *28*, 10278–10286. https://doi.org/10.1523/JNEUROSCI.2451-08.2008

Schanzenbächer, C.T., Langer, J.D., Schuman, E.M., 2018. Time- and polarity-dependent proteomic changes associated with homeostatic scaling at central synapses. eLife *7*, e33322. https://doi.org/10.7554/eLife.33322

Schanzenbächer, C.T., Sambandan, S., Langer, J.D., Schuman, E.M., 2016. Nascent Proteome Remodeling following Homeostatic Scaling at Hippocampal Synapses. Neuron *92*, 358–371. https://doi.org/10.1016/j.neuron.2016.09.058

Schaukowitch, K., Reese, A.L., Kim, S.-K., Kilaru, G., Joo, J.-Y., Kavalali, E.T., Kim, T.-K., 2017. An Intrinsic Transcriptional Program Underlying Synaptic Scaling during Activity Suppression. Cell Rep. *18*, 1512–1526. https://doi.org/10.1016/j.celrep.2017.01.033

Sohal, V.S., Rubenstein, J.L.R., 2019. Excitation-inhibition balance as a framework for investigating mechanisms in neuropsychiatric disorders. Mol. Psychiatry *24*, 1248–1257. https://doi.org/10.1038/s41380-019-0426-0

Steinmetz, C.C., Tatavarty, V., Sugino, K., Shima, Y., Joseph, A., Lin, H., Rutlin, M., Lambo, M., Hempel, C.M., Okaty, B.W., Paradis, S., Nelson, S.B., Turrigiano, G.G., 2016. Upregulation of μ3A Drives Homeostatic Plasticity by Rerouting AMPAR into the Recycling Endosomal Pathway. Cell Rep. *16*, 2711–2722. https://doi.org/10.1016/j.celrep.2016.08.009

Steinmetz, C.C., Turrigiano, G.G., 2010. Tumor Necrosis Factor-α Signaling Maintains the Ability of Cortical Synapses to Express Synaptic Scaling. J. Neurosci. *30*, 14685–14690. https://doi.org/10.1523/JNEUROSCI.2210-10.2010

Stellwagen, D., Malenka, R.C., 2006. Synaptic scaling mediated by glial TNF-α. Nature *440*, 1054–1059. https://doi.org/10.1038/nature04671

Sutton, M.A., Ito, H.T., Cressy, P., Kempf, C., Woo, J.C., Schuman, E.M., 2006. Miniature Neurotransmission Stabilizes Synaptic Function via Tonic Suppression of Local Dendritic Protein Synthesis. Cell *125*, 785–799. https://doi.org/10.1016/j.cell.2006.03.040

Tan, H.L., Queenan, B.N., Huganir, R.L., 2015. GRIP1 is required for homeostatic regulation of AMPAR trafficking. PNAS *112*, 10026–10031. https://doi.org/10.1073/pnas.1512786112

Tatavarty, V., Torrado Pacheco, A., Groves Kuhnle, C., Lin, H., Koundinya, P., Miska, N.J., Hengen, K.B., Wagner, F.F., Van Hooser, S.D., Turrigiano, G.G., 2020. Autism-Associated Shank3 Is Essential for Homeostatic Compensation in Rodent V1. Neuron *106*, 769-777.e4. https://doi.org/10.1016/j.neuron.2020.02.033

Torrado Pacheco, A., Bottorff, J., Gao, Y., Turrigiano, G.G., 2021. Sleep Promotes Downward Firing Rate Homeostasis. Neuron *109*, 530-544.e6. https://doi.org/10.1016/j.neuron.2020.11.001

Torrado Pacheco, A., Tilden, E.I., Grutzner, S.M., Lane, B.J., Wu, Y., Hengen, K.B., Gjorgjieva, J., Turrigiano, G.G., 2019. Rapid and active stabilization of visual cortical firing rates across light–dark transitions. PNAS *116*, 18068–18077. https://doi.org/10.1073/pnas.1906595116

Toyoizumi, T., Kaneko, M., Stryker, M.P., Miller, K.D., 2014. Modeling the Dynamic Interaction of Hebbian and Homeostatic Plasticity. Neuron *84*, 497–510. https://doi.org/10.1016/j.neuron.2014.09.036

Trojanowski, N.F., Turrigiano, G.G., 2021. CaMKIV Signaling Is Not Essential for the Maintenance of Intrinsic or Synaptic Properties in Mouse Visual Cortex. eNeuro *8*. https://doi.org/10.1523/ENEURO.0135-21.2021

Turrigiano, G., 2012. Homeostatic synaptic plasticity: local and global mechanisms for stabilizing neuronal function. Cold Spring Harb. Perspect. Biol. *4*, a005736. https://doi.org/10.1101/cshperspect.a005736

Turrigiano, G., 2011. Too Many Cooks? Intrinsic and Synaptic Homeostatic Mechanisms in Cortical Circuit Refinement. Annu. Rev. Neurosci. *34*, 89–103. https://doi.org/10.1146/annurev-neuro-060909-153238

Turrigiano, G.G., Leslie, K.R., Desai, N.S., Rutherford, L.C., Nelson, S.B., 1998. Activity-dependent scaling of quantal amplitude in neocortical neurons. Nature *391*, 892–896. https://doi.org/10.1038/36103

Turrigiano, G.G., Nelson, S.B., 2004. Homeostatic plasticity in the developing nervous system. Nat. Rev. Neurosci. *5*, 97–107. https://doi.org/10.1038/nrn1327

Valakh, V., Wise, D., Zhu, X.A., Sha, M., Fok, J., Van Hooser, S.D., Schectman, R., Cepeda, I., Kirk, R., O'Toole, S.M., Nelson, S.B., 2023. A transcriptional constraint mechanism limits the homeostatic response to activity deprivation in mammalian neocortex. eLife *12*, e74899. https://doi.org/10.7554/eLife.74899

Watt, A.J., Rossum, M.C.W. van, MacLeod, K.M., Nelson, S.B., Turrigiano, G.G., 2000. Activity Coregulates Quantal AMPA and NMDA Currents at Neocortical Synapses. Neuron *26*, 659–670. https://doi.org/10.1016/S0896-6273(00)81202-7

Wen, W., Turrigiano, G.G., 2024. Keeping Your Brain in Balance: Homeostatic Regulation of Network Function. Annu. Rev. Neurosci. *47*, null. https://doi.org/10.1146/annurev-neuro-092523-110001

Wen, W., Turrigiano, G.G., 2021. Developmental Regulation of Homeostatic Plasticity in Mouse Primary Visual Cortex. J. Neurosci. *41*(48), 9891-9905. https://doi.org/10.1523/JNEUROSCI.1200-21.2021

Wierenga, C.J., Ibata, K., Turrigiano, G.G., 2005. Postsynaptic Expression of Homeostatic Plasticity at Neocortical Synapses. J. Neurosci. *25*, 2895–2905. https://doi.org/10.1523/JNEUROSCI.5217-04.2005

Wu, Y.K., Hengen, K.B., Turrigiano, G.G., Gjorgjieva, J., 2020. Homeostatic mechanisms regulate distinct aspects of cortical circuit dynamics. PNAS *117*, 24514–24525. https://doi.org/10.1073/pnas.1918368117

Zbili, M., Rama, S., Benitez, M.-J., Fronzaroli-Molinieres, L., Bialowas, A., Boumedine-Guignon, N., Garrido, J.J., Debanne, D., 2021. Homeostatic regulation of axonal Kv1.1 channels accounts for both synaptic and intrinsic modifications in the hippocampal CA3 circuit. PNAS *118*. https://doi.org/10.1073/pnas.2110601118

Figure 1

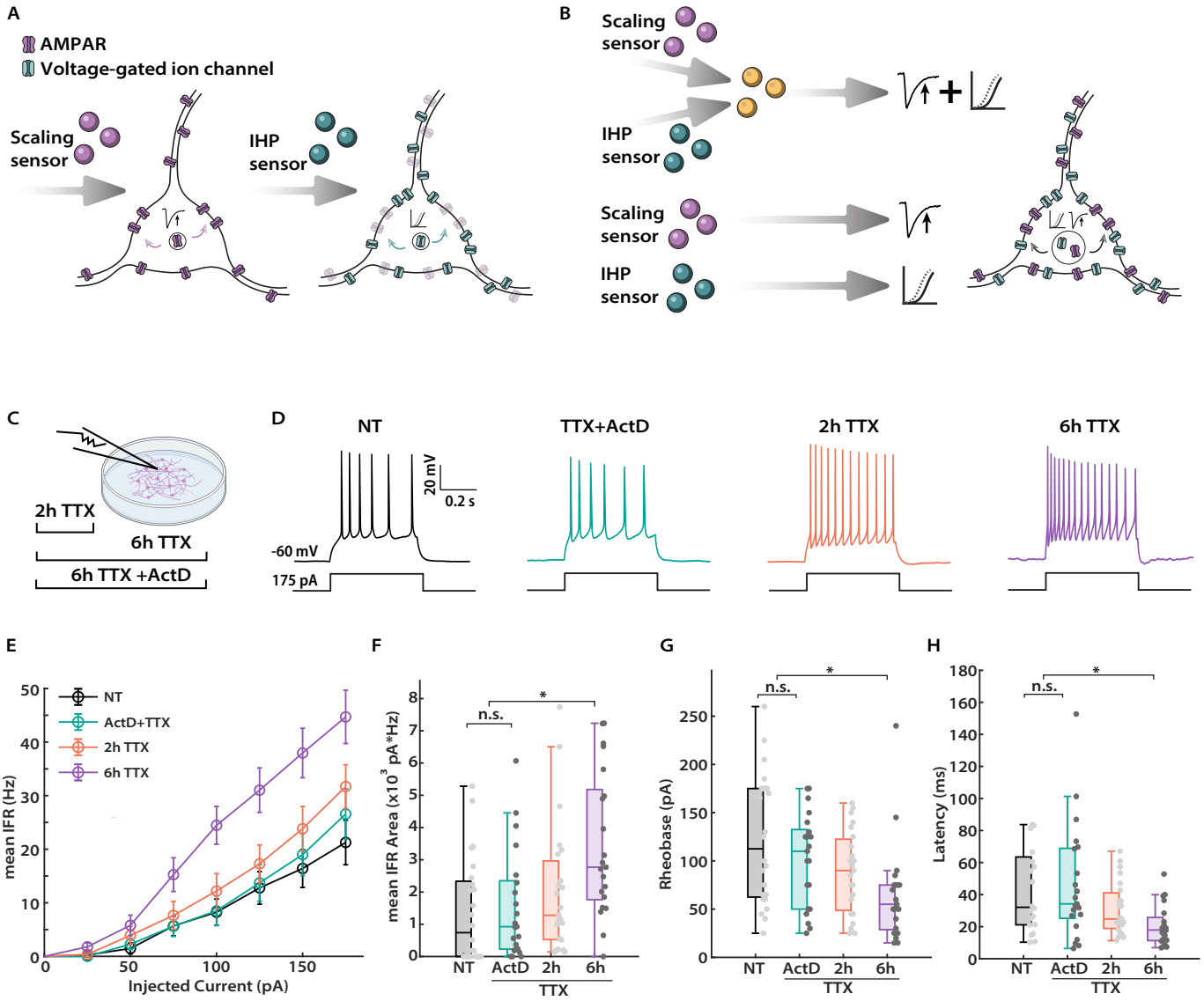
A
AMPAR
Voltage-gated ion channel
Scaling sensor
IHP sensor
B
Scaling sensor
IHP sensor
Scaling sensor
IHP sensor
C
2h TTX
6h TTX
6h TTX +ActD
D
NT
TTX+ActD
2h TTX
6h TTX
20 mV
0.2 s
-60 mV
175 pA
E
NT
ActD+TTX
2h TTX
6h TTX
mean IFR (Hz)
Injected Current (pA)
F
mean IFR Area (x10^3 pA*Hz)
n.s.
*
NT
ActD
2h
6h
TTX
G
Rheobase (pA)
n.s.
*
NT
ActD
2h
6h
TTX
H
Latency (ms)
n.s.
*
NT
ActD
2h
6h
TTX

Figure 1. IHP is rapidly induced by TTX-mediated activity silencing and requires transcription.

(A) and (B) Two proposed models for the coordination of synaptic scaling and IHP in neocortical circuits. (A) depicts a sequential model where synaptic scaling occurs prior to and is required for IHP induction. Alternatively, in (B), synaptic scaling and IHP are arranged in parallel and responsive to distinct activity sensors. Note that the intracellular processes controlling the expression of plasticity could converge (upper) or to stay separated (lower).

(C) Experimental paradigm. Cultured neocortical neurons were treated with TTX for either 2 or 6 hours before electrophysiological recording. To assess whether IHP expression requires gene transcription, neurons were also co-treated with TTX and Actinomycin D (ActD) for 6 hours.

(D) Representative traces of spike trains evoked by current injections in cultured pyramidal neurons from the indicated conditions.

(E) Comparison of mean instantaneous firing rate (IFR) vs. current injection (F-I) curves from the indicated conditions. NT, $n = 24$; ActD, $n = 21$; 2h, $n = 23$; 6h, $n = 21$. For F-I curves here and throughout, data are reported as mean±S.E.M of all cells from each condition.

(F) Comparison of the area under the F-I curve for each neuron from the indicated conditions. Here and throughout, each data point indicates one neuron. Kruskal-Wallis test with Tukey post-hoc correction: NT vs. ActD, $p = 0.9402$; NT vs. 2h, $p = 0.4448$; NT vs. 6h, $p = 0.0021$; ActD vs. 2h, $p = 0.8198$; ActD vs. 6h, $p = 0.0198$; 2h vs. 6h, $p = 0.1566$. Here and below example comparisons are given on plots for clarity; * = $p < 0.05$, ** = $p < 0.01$, *** = $p < 0.001$, n.s. = not significant.

(G) Comparison of rheobase current from the indicated conditions. Kruskal-Wallis test with Tukey post-hoc correction: NT vs. ActD, $p = 0.8467$; NT vs. 2h, $p = 0.3846$; NT vs. 6h, $p = 0.0037$; ActD vs. 2h, $p = 0.8858$; ActD vs. 6h, $p = 0.0590$; 2h vs. 6h, $p = 0.2574$.

(H) Comparison of latency to the first spike for 175 pA of current injection from the indicated conditions. Kruskal-Wallis test with Tukey post-hoc correction: NT vs. ActD, $p = 1.0$; NT vs. 2h, $p = 0.7056$; NT vs. 6h, $p = 0.0132$; ActD vs. 2h, $p = 0.6881$; ActD vs. 6h, $p = 0.0112$; 2h vs. 6h, $p = 0.1673$.

Figure 2

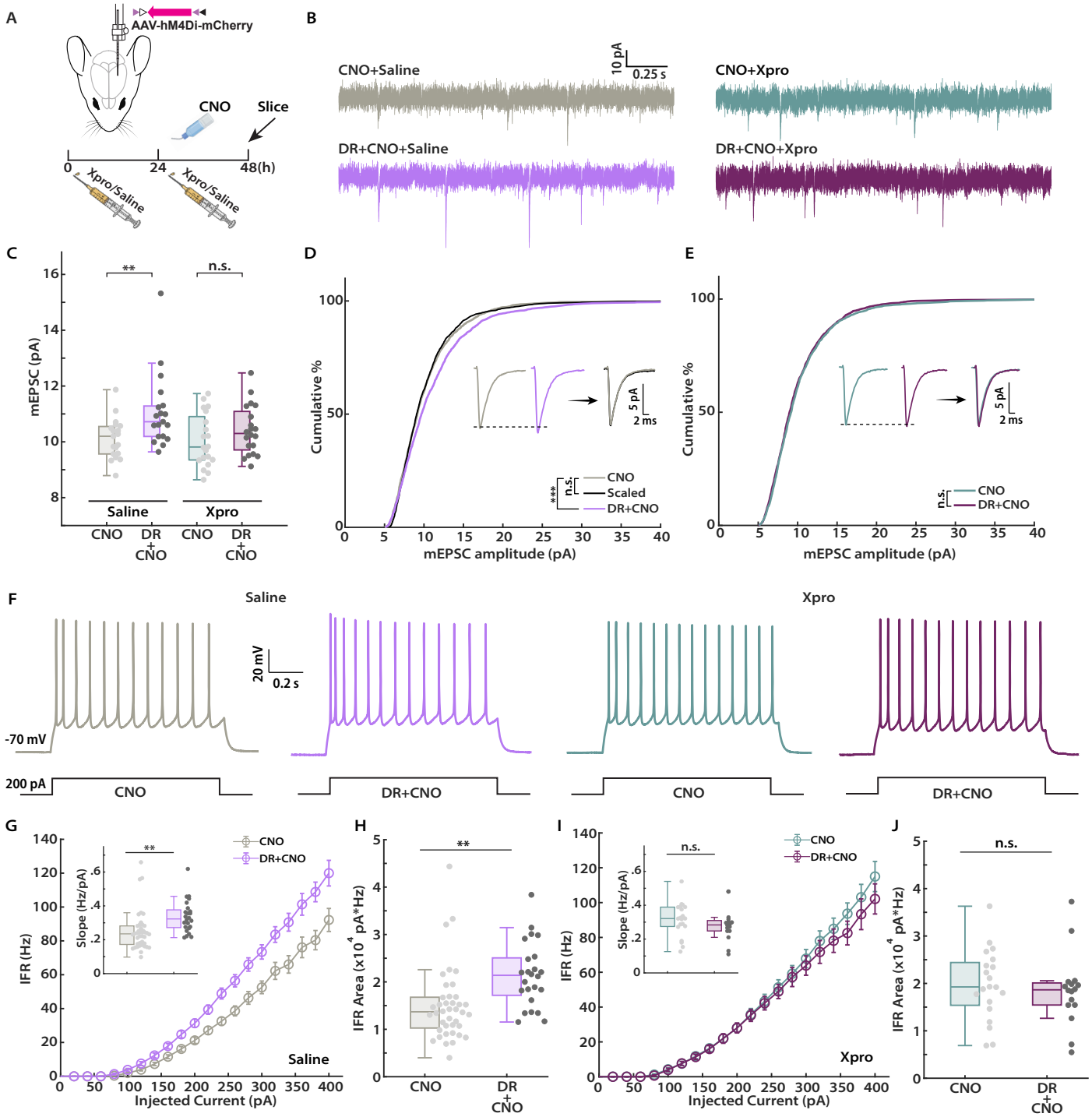
A
AAV-hM4Di-mCherry
CNO
Slice
0
24
48(h)
Xpro/Saline
Xpro/Saline
B
CNO+Saline
10 pA
0.25 s
CNO+Xpro
DR+CNO+Saline
DR+CNO+Xpro
C
mEPSC (pA)
**
n.s.
Saline
Xpro
CNO
DR + CNO
CNO
DR + CNO
D
Cumulative %
mEPSC amplitude (pA)
5 pA
2 ms
***
n.s.
CNO
Scaled
DR+CNO
E
Cumulative %
mEPSC amplitude (pA)
5 pA
2 ms
n.s.
CNO
DR+CNO
F
Saline
Xpro
20 mV
0.2 s
-70 mV
200 pA
CNO
DR+CNO
CNO
DR+CNO
G
IFR (Hz)
Slope (Hz/pA)
**
CNO
DR+CNO
Saline
Injected Current (pA)
H
IFR Area (x10^4 pA*Hz)
**
CNO
DR + CNO
I
IFR (Hz)
Slope (Hz/pA)
n.s.
CNO
DR+CNO
Xpro
Injected Current (pA)
J
IFR Area (x10^4 pA*Hz)
n.s.
CNO
DR + CNO

Figure 2. IHP expression in V1 L2/3 pyramidal neurons requires tumor necrosis factor α (TNFα) signaling.

(A) Experimental paradigm (adapted from Wen and Turrigiano 2021). Viruses carrying hM4Di (DR) were unilaterally delivered into mouse V1 during P14-16. Animals were administered either Xpro or saline 24 hours before receiving CNO, and again when CNO was commenced. CNO was administered via drinking water for 24 hours before animals were sacrificed for slice electrophysiological recordings (during P25-30). Icons adapted from Biorender.com.

(B) Representative traces of mEPSC recordings from the indicated conditions.

(C) Comparison of the mean mEPSC amplitude for L2/3 pyramidal neurons from the indicated conditions. Saline, n = 19 from 6 animals for both CNO and DR+CNO conditions; Xpro, n = 20 from 5 animals for both CNO and DR+CNO conditions. Unpaired T test: Saline, CNO vs. DR+CNO, p = 0.0063; Xpro, CNO vs. DR+CNO, p = 0.1404.

(D) Cumulative distribution of mEPSC amplitudes for animals treated with saline. Population amplitudes from DR+CNO condition are scaled according to the linear function y = 1.31x – 2.16 (black curve). Inset: Left, unscaled average waveforms of CNO and DR+CNO conditions, respectively; Right, overlay of the average waveforms from CNO and scaled (black trace) populations, respectively. Kolmogorov-Smirnov test: CNO vs. DR+CNO, p = 1.20E-7; CNO vs. Scaled, p = 0.4216.

(E) Same as D, but for animals treated with Xpro. Inset: Left, unscaled average waveforms of CNO and DR+CNO conditions, respectively; Right, overlay of the unscaled average waveforms from CNO and DR+CNO conditions, respectively. Kolmogorov-Smirnov test: CNO vs. DR+CNO, p = 0.3649.

(F) Representative traces of spike trains evoked by current injections in L2/3 pyramidal neurons from the indicated conditions.

(G) Comparison of F-I curves for the CNO and DR+CNO groups from animals treated with saline. CNO, n = 40, 8 animals; DR+CNO, n = 24, 5 animals. Inset: Comparison of the F-I curve slope (linear part) for both conditions. Unpaired T test: CNO vs. DR+CNO, p = 0.0037.

(H) Comparison of the area under F-I curve for each neuron from the indicated conditions. Unpaired T test: CNO vs. DR+CNO, p = 0.0011.

(I) Same as G, but for animals treated with Xpro. CNO, n = 20, 4 animals; DR+CNO, n = 16, 3 animals. Inset: Comparison of the F-I curve slope (linear part) for both conditions. Unpaired T test: CNO vs. DR+CNO, p = 0.1661.

(J) Same as H, but for animals treated with Xpro. Unpaired T test: CNO vs. DR+CNO, p = 0.4544.

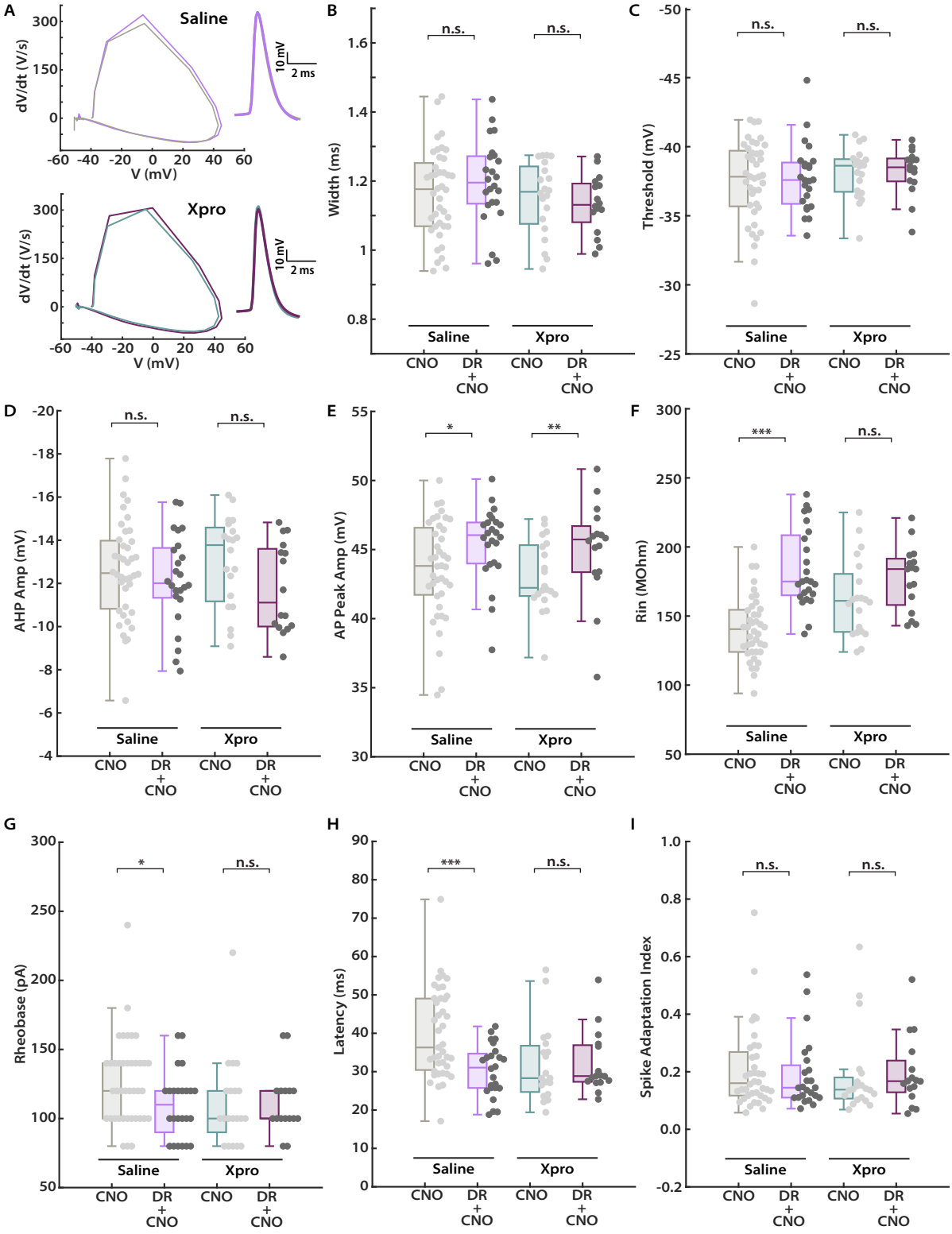
A
Saline
Xpro
dV/dt (V/s)
V (mV)
10 mV
2 ms
B
Width (ms)
C
Threshold (mV)
D
AHP Amp (mV)
E
AP Peak Amp (mV)
F
Rin (MOhm)
G
Rheobase (pA)
H
Latency (ms)
I
Spike Adaptation Index
n.s.
*
**
***
Saline
Xpro
CNO
DR + CNO

Figure 3. Cellular and spike parameters following IHP induction in V1 L2/3 pyramidal neurons.

(A) Phase plane plots (left, action potential plotted as dV/dt vs. membrane potential) for the average waveforms (right, overlay of both CNO and DR+CNO conditions) of the first spike evoked at rheobase from animals treated with saline (upper) and Xpro (lower), respectively.

(B) Comparison of full width at half-maximum for the first spike at rheobase from the indicated conditions. Unpaired T test: Saline, CNO vs. DR+CNO, $p = 0.3956$; Xpro, CNO vs. DR+CNO, $p = 0.4169$.

(C) Comparison of action potenial voltage threshold for the first spike at rheobase from the indicated conditions. Unpaired T test: Saline, CNO vs. DR+CNO, $p = 0.6735$; Xpro, CNO vs. DR+CNO, $p = 0.8112$.

(D) Comparison of afterhyperpolarization amplitude for the first spike at rheobase from the indicated conditions. Unpaired T test: Saline, CNO vs. DR+CNO, $p = 0.3861$; Xpro, CNO vs. DR+CNO, $p = 0.1079$.

(E) Comparison of spike peak amplitude for the first spike at rheobase from the indicated conditions. Mann-Whitney U test: Saline, CNO vs. DR+CNO, $p = 0.0311$; Xpro, CNO vs. DR+CNO, $p = 0.0416$.

(F) Comparison of neuronal input resistance from the indicated conditions. Unpaired T test: Saline, CNO vs. DR+CNO, $p = 6.03E-7$; Xpro, CNO vs. DR+CNO, $p = 0.0745$.

(G) Comparison of rheobase current from the indicated conditions. Unpaired T test: Saline, CNO vs. DR+CNO, $p = 0.0337$; Xpro, CNO vs. DR+CNO, $p = 0.6901$.

(H) Comparison of latency to the first spike at 200 pA of current injection from the indicated conditions. Mann-Whitney U test: Saline, CNO vs. DR+CNO, $p = 5.23E-4$; Xpro, CNO vs. DR+CNO, $p = 0.5962$.

(I) Comparison of spike frequency adaptation at 400 pA of current injection from the indicated conditions. Mann-Whitney U test: Saline, CNO vs. DR+CNO, $p = 0.6522$; Xpro, CNO vs. DR+CNO, $p = 0.3159$.

A through I: same sample sizes as shown in Figures 2G and 2I.

Figure 4

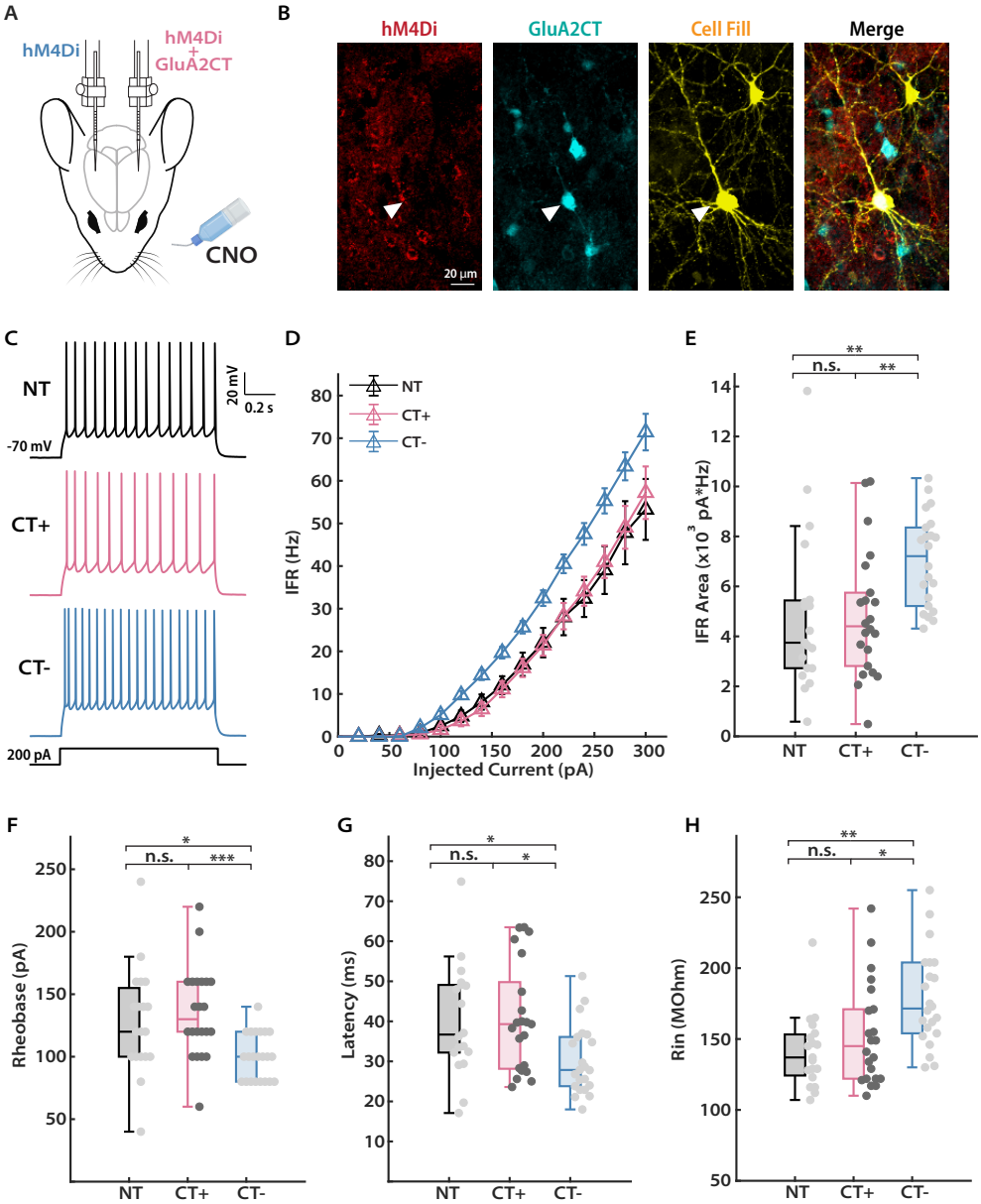
A
hM4Di
hM4Di + GluA2CT
CNO
B
hM4Di
GluA2CT
Cell Fill
Merge
20 µm
C
NT
-70 mV
20 mV
0.2 s
CT+
CT-
200 pA
D
NT
CT+
CT-
IFR (Hz)
Injected Current (pA)
E
n.s.
**
**
IFR Area (x10^3 pA*Hz)
NT
CT+
CT-
F
n.s.
*
***
Rheobase (pA)
NT
CT+
CT-
G
n.s.
*
*
Latency (ms)
NT
CT+
CT-
H
n.s.
**
*
Rin (MOhm)
NT
CT+
CT-

Figure 4. IHP in V1 L2/3 pyramidal neurons is prevented by expression of the GluA2 C-terminal fragment (CT).

(A) Experimental paradigm (Wen and Turrigiano 2021). Viruses carrying the inhibitory DREADD hM4Di and GluA2 CT were mixed before being delivered unilaterally into mouse V1 during P14-16 (CT+), while only hM4Di was delivered into the other hemisphere to serve as a within-animal positive control (CT-). CNO was administered orally via drinking water for 24 hours before mice were sacrificed for slice electrophysiological recordings, which were performed during P25-30. Icons adapted from Biorender.com.

(B) Representative images of a L2/3 pyramidal neurons recorded under the CT+ condition. The cell shows co-expression of hM4Di (tagged by mCherry) and GluA2 CT (tagged by GFP). White triangles indicate the recorded cell. Scale bar: 20 μm.

(C) Representative traces of spike trains evoked by current injections in L2/3 pyramidal neurons for the indicated conditions. NT indicates littermates that received neither CNO nor virus injection.

(D) Comparison of F-I curves of L2/3 pyramidal neurons from the indicated conditions. NT, n = 19, 3 animals; CT+, n = 22, 7 animals; CT-, n = 22, 7 animals.

(E) Comparison of the area under F-I curve for each neuron from the indicated conditions. Kruskal-Wallis test with Tukey post-hoc correction: NT vs. CT+, p = 0.9546; NT vs. CT-, p = 0.0047; CT+ vs. CT-, p = 0.0084.

(F) Comparison of rheobase current from the indicated conditions. Kruskal-Wallis test with Tukey post-hoc correction: NT vs. CT+, p = 0.7482; NT vs. CT-, p = 0.0153; CT+ vs. CT-, p = 8.15E-4.

(G) Comparison of latency to the first spike at 200 pA of current injection from the indicated conditions. Kruskal-Wallis test with Tukey post-hoc correction: NT vs. CT+, p = 0.9998; NT vs. CT-, p = 0.0286; CT+ vs. CT-, p = 0.0202.

(H) Comparison of neuronal input resistance from the indicated conditions. Kruskal-Wallis test with Tukey post-hoc correction: NT vs. CT+, p = 0.5887; NT vs. CT-, p = 0.0010; CT+ vs. CT-, p = 0.0193.

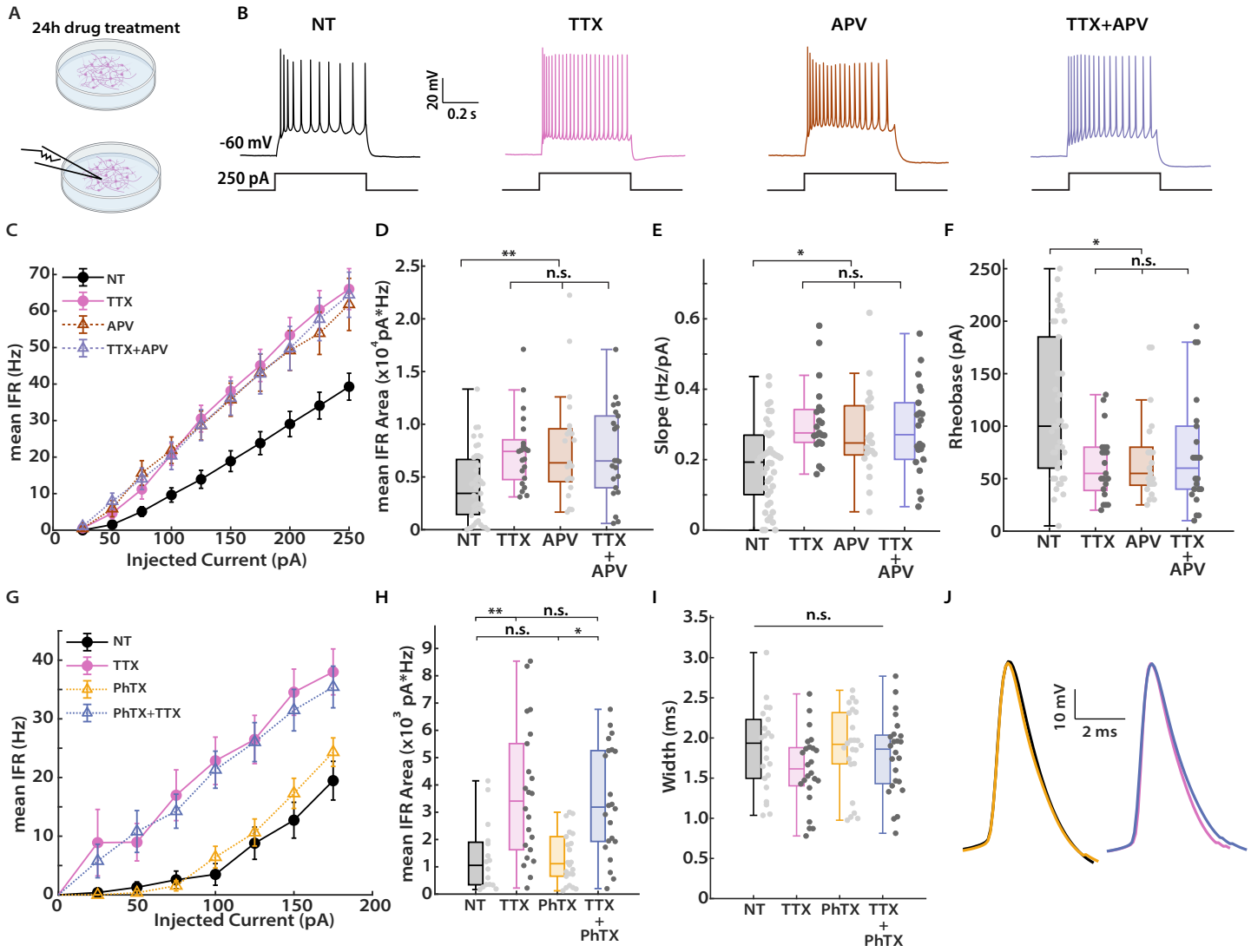
A
24h drug treatment
B
NT
TTX
APV
TTX+APV
-60 mV
250 pA
20 mV
0.2 s
C
NT
TTX
APV
TTX+APV
mean IFR (Hz)
Injected Current (pA)
D
mean IFR Area (x10^4 pA*Hz)
**
n.s.
NT
TTX
APV
TTX + APV
E
Slope (Hz/pA)
*
n.s.
F
Rheobase (pA)
*
n.s.
G
NT
TTX
PhTX
PhTX+TTX
mean IFR (Hz)
Injected Current (pA)
H
mean IFR Area (x10^3 pA*Hz)
**
n.s.
n.s.
*
NT
TTX
PhTX
TTX + PhTX
I
Width (ms)
n.s.
J
10 mV
2 ms

Figure 5. Synaptic scaling and IHP can be independently induced by suppressing spikes and NMDAR signaling, respectively.

(A) Experimental paradigm for assessing effects of activity manipulation on homeostatic plasticity in cultured neocortical neurons. Electrophysiological recordings were performed after 24 hours of drug treatment.

(B) Representative traces of spike trains evoked by current injections in cultured pyramidal neurons following treatments of TTX, APV, or TTX+APV.

(C) Comparison of F-I curves for pyramidal neurons from the indicated conditions. NT, n = 42; TTX, n = 21; APV, n = 21; TTX+APV, n = 22.

(D) Comparison of the area under F-I curve for each neuron from the indicated conditions. Kruskal-Wallis test with Tukey post-hoc correction: NT vs. TTX, p = 0.0037; NT vs. APV, p = 0.0132; NT vs. TTX+APV, p = 0.0076; TTX vs. APV, p = 0.9883; TTX vs. TTX+APV, p = 0.9961; APV vs. TTX+APV, p = 0.9996.

(E) Comparison of F-I curve slope from the indicated conditions. Kruskal-Wallis test with Tukey post-hoc correction: NT vs. TTX, p = 0.0010; NT vs. APV, p = 0.0330; NT vs. TTX+APV, p = 0.0170; TTX vs. APV, p = 0.7265; TTX vs. TTX+APV, p = 0.8801; APV vs. TTX+APV, p = 0.9898.

(F) Comparison of rheobase current from the indicated conditions. Kruskal-Wallis test with Tukey post-hoc correction: NT vs. TTX, p = 0.0219; NT vs. APV, p = 0.0385; NT vs. TTX+APV, p = 0.0374; TTX vs. APV, p = 0.9983; TTX vs. TTX+APV, p = 0.9973; APV vs. TTX+APV, p = 0.9999.

(G) Comparison of F-I curves from the indicated conditions. NT, n = 22; PhTX, n = 24; TTX, n = 24; PhTX+TTX, n =24.

(H) Comparison of the area under F-I curve for each neuron from the indicated conditions. Kruskal-Wallis test with Tukey post-hoc correction: NT vs. PhTX, p = 0.8311; NT vs. TTX, p = 0.0011; NT vs. PhTX+TTX, p = 0.0014; PhTX vs. TTX, p = 0.0173; PhTX vs. PhTX+TTX, p = 0.0210; TTX vs. PhTX+TTX, p = 0.9999.

(I) Comparison of full width at half-maximum for the first spike at rheobase from the indicated conditions. Kruskal-Wallis test: p = 0.1815.

(J) Overlay of the average waveforms from first spikes evoked at rheobase. Left, NT vs. PhTX; Right, TTX vs. PhTX+TTX.

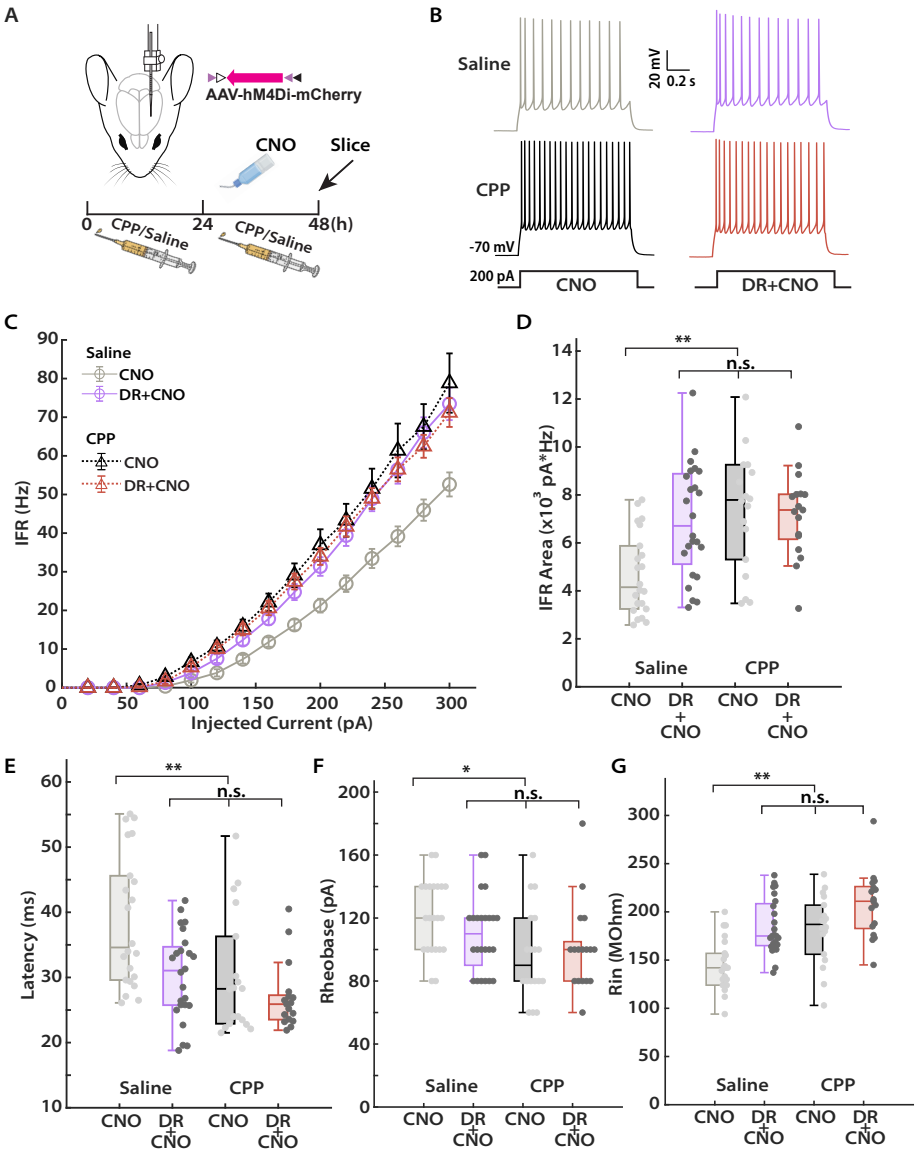
A
AAV-hM4Di-mCherry
CNO
Slice
0
24
48(h)
CPP/Saline
CPP/Saline
B
Saline
20 mV
0.2 s
CPP
-70 mV
200 pA
CNO
DR+CNO
C
Saline
CNO
DR+CNO
CPP
CNO
DR+CNO
IFR (Hz)
Injected Current (pA)
D
**
n.s.
IFR Area (x10³ pA*Hz)
Saline
CPP
CNO
DR + CNO
CNO
DR + CNO
E
**
n.s.
Latency (ms)
F
*
n.s.
Rheobase (pA)
G
**
n.s.
Rin (MOhm)

Figure 6. Chronic treatment with an NMDAR antagonist induces IHP in V1 L2/3 pyramidal neurons.

(A) Experimental paradigm. Similar to the one performed in the Xpro treatment (Figure 2A), but with the NMDAR antagonist CPP instead.

(B) Representative traces of spike trains evoked by current injections in L2/3 pyramidal neurons for the indicated conditions.

(C) Comparison of F-I curves for L2/3 pyramidal neurons from the indicated conditions. Saline-CNO, n = 22, 5 animals; Saline-DR+CNO, n = 24, 5 animals; CPP-CNO, n = 18, 4 animals; CPP-DR+CNO, n = 17, 4 animals.

(D) Comparison of the area under F-I curve for each neuron from the indicated conditions. One-way ANOVA test with Tukey post-hoc correction: Saline-CNO vs. Saline-DR+CNO, p = 0.0083; Saline-CNO vs. CPP-CNO, p = 4.36E-4; Saline-CNO vs. CPP-DR+CNO, p = 0.0067; Saline-DR+CNO vs. CPP-CNO, p = 0.6571; Saline-DR+CNO vs. CPP-DR+CNO, p = 0.9839; CPP-CNO vs. CPP-DR+CNO, p = 0.8860.

(E) Comparison of latency to the first spike at 200 pA of current injection from the indicated conditions. Kruskal-Wallis test with Tukey post-hoc correction: Saline-CNO vs. Saline-DR+CNO, p = 0.0346; Saline-CNO vs. CPP-CNO, p = 0.0111; Saline-CNO vs. CPP-DR+CNO, p = 3.40E-4; Saline-DR+CNO vs. CPP-CNO, p = 0.9380; Saline-DR+CNO vs. CPP-DR+CNO, p = 0.3923; CPP-CNO vs. CPP-DR+CNO, p = 0.7820.

(F) Comparison of rheobase current from the indicated conditions. Kruskal-Wallis test with Tukey post-hoc correction: Saline-CNO vs. Saline-DR+CNO, p = 0.0337; Saline-CNO vs. CPP-CNO, p = 0.0026; Saline-CNO vs. CPP-DR+CNO, p = 0.0128; Saline-DR+CNO vs. CPP-CNO, p = 0.4014; Saline-DR+CNO vs. CPP-DR+CNO, p = 0.6462; CPP-CNO vs. CPP-DR+CNO, p = 0.9862.

(G) Comparison of neuronal input resistance from the indicated conditions. Kruskal-Wallis test with Tukey post-hoc correction: Saline-CNO vs. Saline-DR+CNO, p = 2.03E-4; Saline-CNO vs. CPP-CNO, p = 0.0014; Saline-CNO vs. CPP-DR+CNO, p = 7.54E-8; Saline-DR+CNO vs. CPP-CNO, p = 0.9947; Saline-DR+CNO vs. CPP-DR+CNO, p = 0.0863; CPP-CNO vs. CPP-DR+CNO, p = 0.0723.

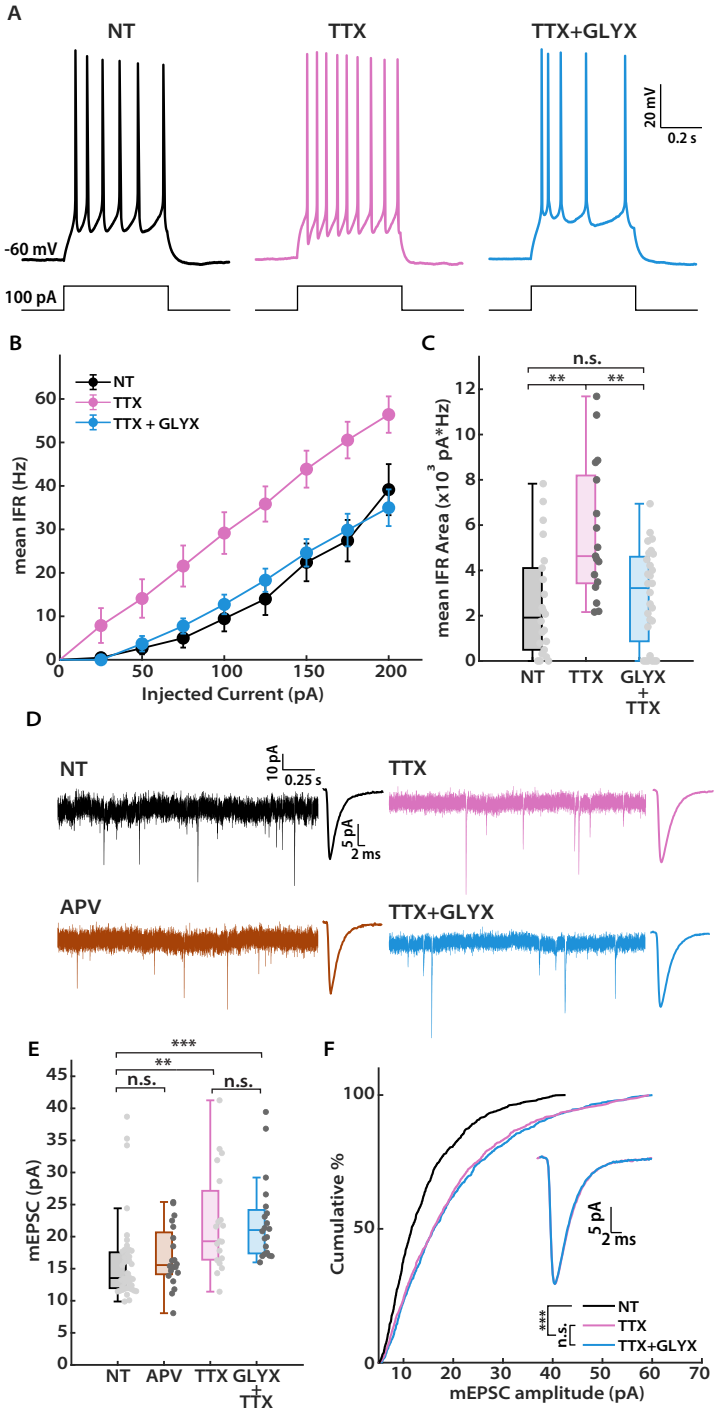
A
NT
TTX
TTX+GLYX
20 mV
0.2 s
-60 mV
100 pA
B
NT
TTX
TTX + GLYX
mean IFR (Hz)
Injected Current (pA)
C
n.s.
**
**
mean IFR Area (x10^3 pA*Hz)
NT
TTX
GLYX + TTX
D
NT
10 pA
0.25 s
5 pA
2 ms
TTX
APV
TTX+GLYX
E
***
**
n.s.
n.s.
mEPSC (pA)
NT
APV
TTX
GLYX + TTX
F
Cumulative %
5 pA
2 ms
***
n.s.
NT
TTX
TTX+GLYX
mEPSC amplitude (pA)

Figure 7. IHP, but not synaptic scaling, can be suppressed through enhancement of NMDAR signaling.

(A) Representative traces of spike trains evoked by current injections in cultured pyramidal neurons from the indicated conditions.

(B) Comparison of F-I curves for pyramidal neurons from the indicated conditions. NT, n = 22; TTX, n = 17; TTX+GLYX, n = 28.

(C) Comparison of the area under F-I curve for each neuron from the indicated conditions. Kruskal-Wallis test with Tukey post-hoc correction: NT vs. TTX, p = 0.0100; NT vs. TTX+GLYX, p = 0.7960; TTX vs. TTX+GLYX, p = 0.0024.

(D) Representative traces of mEPSC recordings from the indicated conditions. The average waveform of mEPSC events is shown on the right of the corresponding recording trace.

(E) Comparison of the mean mEPSC amplitude for pyramidal neurons from the indicated conditions. NT, n = 43; APV, n = 20; TTX, n = 19; TTX+GLYX, n = 20. Kruskal-Wallis test with Tukey post-hoc correction: NT vs. APV, p = 0.6221; NT vs. TTX, p = 0.0015; NT vs. TTX+GLYX, p = 3.40E-5; APV vs. TTX, p = 0.0533; APV vs. TTX+GLYX, p = 0.0228; TTX vs. TTX+GLYX, p = 0.9021.

(F) Cumulative distribution of mEPSC amplitudes. Inset: Overlay of unscaled average waveforms from TTX and TTX+GLYX conditions, respectively. Kolmogorov-Smirnov test: NT vs. TTX, p = 4.47E-42; NT vs. TTX+GLYX, p = 3.39E-64; TTX vs. TTX+GLYX, p = 0.1672.

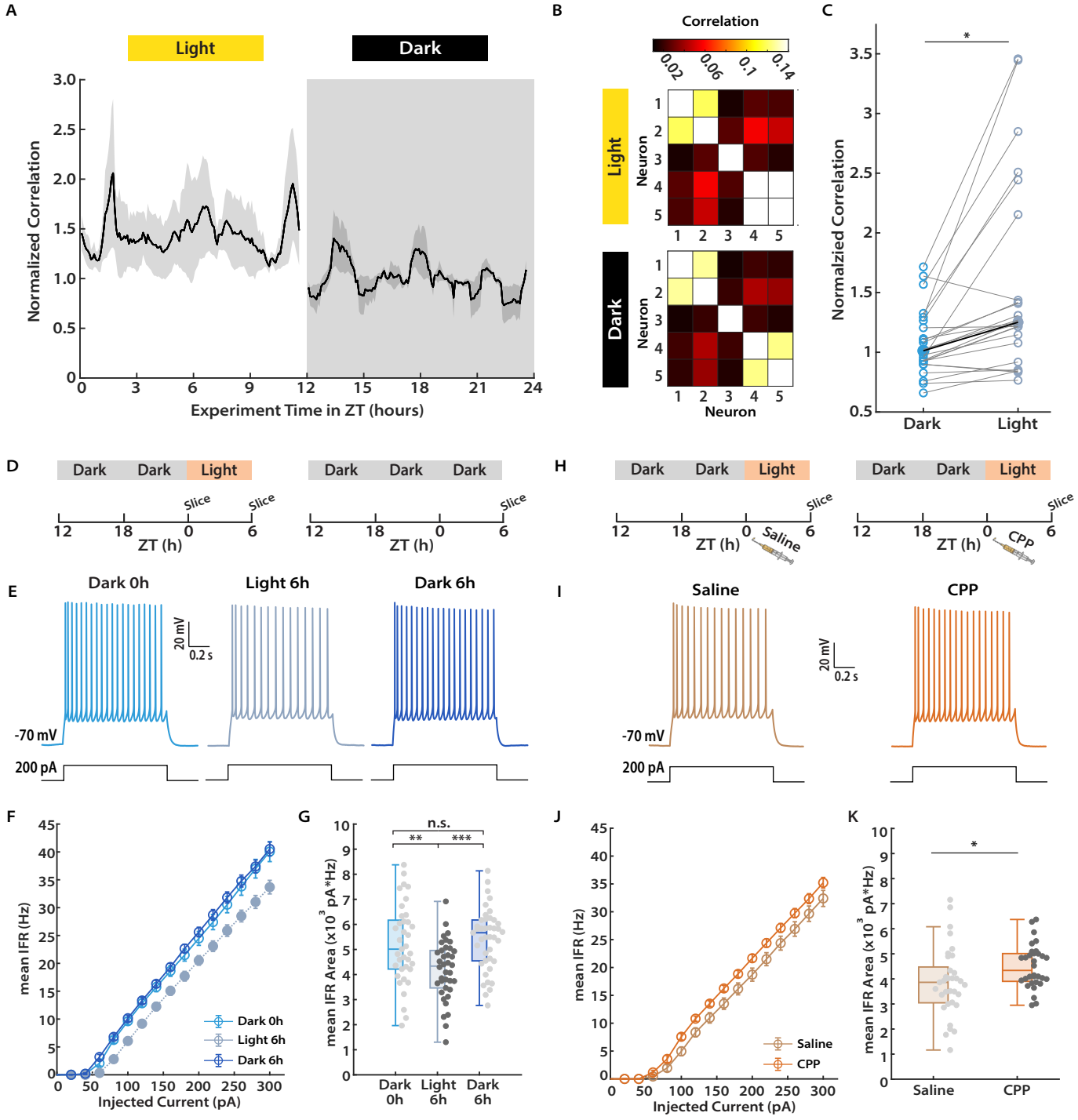
A
Light
Dark
Normalized Correlation
Experiment Time in ZT (hours)
B
Correlation
0.02
0.06
0.1
0.14
Light
Dark
Neuron
C
Normalzied Correlation
Dark
Light
D
Dark Dark Light
Dark Dark Dark
Slice
ZT (h)
E
Dark 0h
Light 6h
Dark 6h
20 mV
0.2 s
-70 mV
200 pA
F
mean IFR (Hz)
Injected Current (pA)
Dark 0h
Light 6h
Dark 6h
G
mean IFR Area (x10^3 pA*Hz)
n.s.
**
***
Dark 0h
Light 6h
Dark 6h
H
Saline
CPP
I
Saline
CPP
J
mean IFR (Hz)
Injected Current (pA)
Saline
CPP
K
mean IFR Area (x10^3 pA*Hz)
Saline
CPP

Figure 8. Synaptic scaling and IHP can be independently recruited during normal sensory experience.

(A) The average correlation in firing for 25 pairs of regular spiking neurons from 5 animals over a day (12 hours light [white] + 12 hours dark [gray]). Correlation values for each pair are normalized to the mean correlation between zeitgeber time (ZT) 900min and ZT 1000 min (when fluctuations in correlation remain relatively low for over an hour). Shaded regions around the correlation trace indicate S.E.M.

(B) Example pairwise correlation matrices of 5 neurons from 1 hemisphere during light (upper) and dark (lower), respectively. Each square in the matrix indicates the correlation value from a pair of neurons.

(C) Comparison of mean normalized correlation across light and dark for all pairs of neurons. Hollow circles connected with grey lines indicate individual pairs, whereas solid circles connected with black lines indicate the medians. Mann-Whitney U test, $p = 0.0244$.

(D) Experimental paradigm for assessing intrinsic excitability of L2/3 pyramidal neurons in mouse V1 across light and dark. Littermates (during P27-32) were sacrificed at ZT 0h (Dark 0h) and ZT 6h (Light 6h) for electrophysiological recordings, respectively (Left). For assessing intrinsic excitability following prolonged dark exposure, animals were kept in dark for another 6 hours from ZT 0h (Dark 6h) before being sacrificed for electrophysiological recordings (Right).

(E) Representative traces of spike trains evoked by current injections in L2/3 pyramidal neurons from the three indicated timepoints in D.

(F) Comparison of F-I curves for L2/3 pyramidal neurons from the three indicated timepoints. Dark 0h, $n = 37$, 4 animals; Light 6h, $n = 38$, 4 animals; Dark 6h, $n = 41$, 4 animals.

(G) Comparison of the area under F-I curve for each neuron from the three indicated timepoints. One-way ANOVA test with Tukey post-hoc correction: Dark 0h vs. Light 6h, $p = 0.0036$; Dark 0h vs. Dark 6h, $p = 0.7634$; Light 6h vs. Dark 6h, $p = 2.32E-4$.

(H) Experimental paradigms for assessing effects of CPP on light-driven reduction in intrinsic excitability. Littermates received either CPP or saline injections at ZT 0h (just before light came on) and were sacrificed for electrophysiological recordings at ZT 6h (after spending 6 hours in the light).

(I) Representative traces of spike trains evoked by current injections in L2/3 pyramidal neurons from the two indicated conditions in H.

(J) Comparison of F-I curves for L2/3 pyramidal neurons from the two indicated conditions in I. CPP, $n = 32$, 3 animals; Saline, $n = 33$, 3 animals.

(K) Comparison of the area under F-I curve for each neuron from the two indicated conditions. Unpaired T test, $p = 0.0166$.

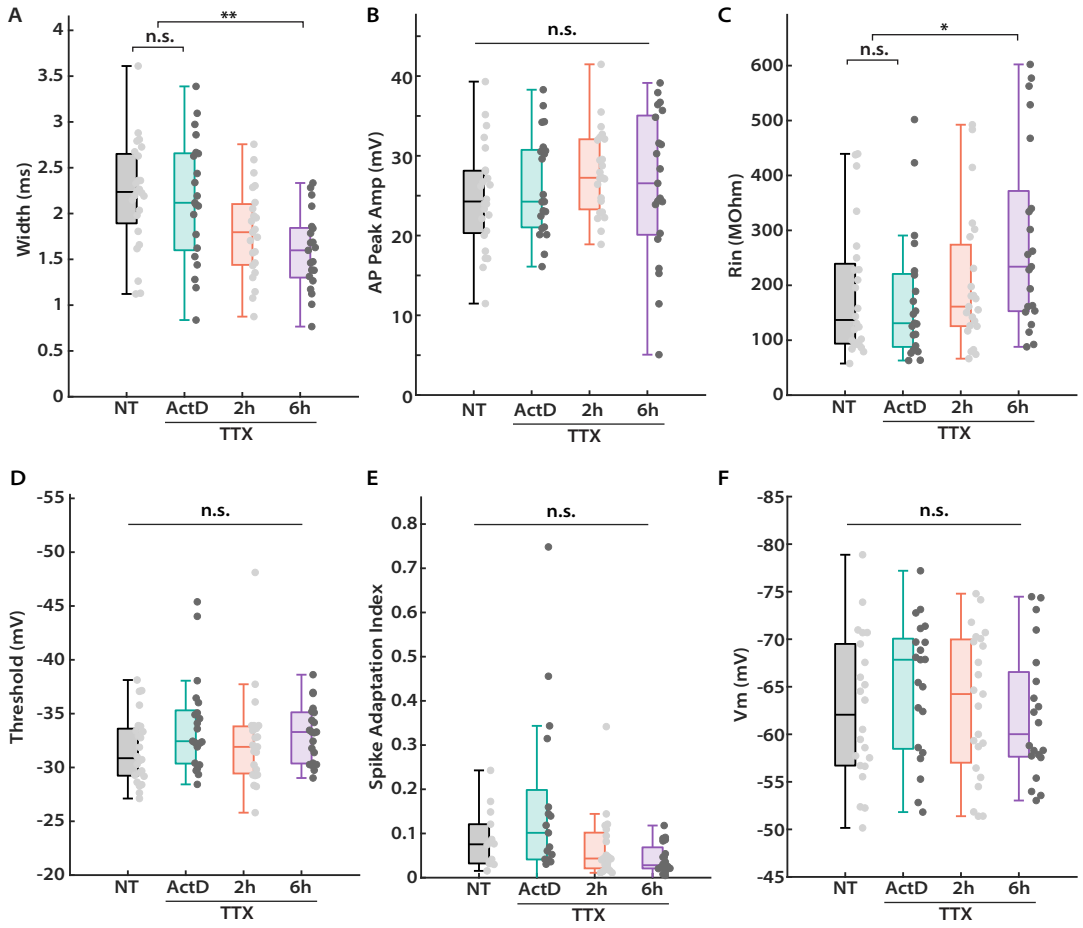
A
Width (ms)
n.s.
**
NT
ActD
2h
6h
TTX
B
AP Peak Amp (mV)
n.s.
C
Rin (MOhm)
n.s.
*
D
Threshold (mV)
n.s.
E
Spike Adaptation Index
n.s.
F
Vm (mV)
n.s.

Figure S1. Cellular properties across the time course of IHP expression in cultured neocortical pyramidal neurons. Related to Figure 1.

(A) Comparison of full width at half-maximum for the first spike at rheobase from the indicated conditions. One-way ANOVA test with Tukey post-hoc correction: NT vs. ActD, $p = 0.9847$; NT vs. 2h, $p = 0.0556$; NT vs. 6h, $p = 0.0017$; ActD vs. 2h, $p = 0.1483$; ActD vs. 6h, $p = 0.0074$; 2h vs. 6h, $p = 0.6036$.

(B) Comparison of the peak amplitude for the first spike at rheobase from the indicated conditions. One-way ANOVA test: $p = 0.5145$.

(C) Comparison of the neuronal input resistance from the indicated conditions. Kruskal-Wallis test with Tukey post-hoc correction: NT vs. ActD, $p = 0.9762$; NT vs. 2h, $p = 0.9260$; NT vs. 6h, $p = 0.0236$; ActD vs. 2h, $p = 0.7450$; ActD vs. 6h, $p = 0.0103$; 2h vs. 6h, $p = 0.3281$.

(D) Comparison of voltage spiking threshold for the first spike at rheobase from the indicated conditions. Kruskal-Wallis test: $p = 0.1736$.

(E) Comparison of spike frequency adaptation at 175 pA of current injection from the indicated conditions. Kruskal-Wallis test: $p = 0.1046$.

(F) Comparison of resting membrane potential from the indicated conditions. One-way ANOVA test: $p = 0.5711$.

A through F: same sample sizes as shown in Figure 1E.

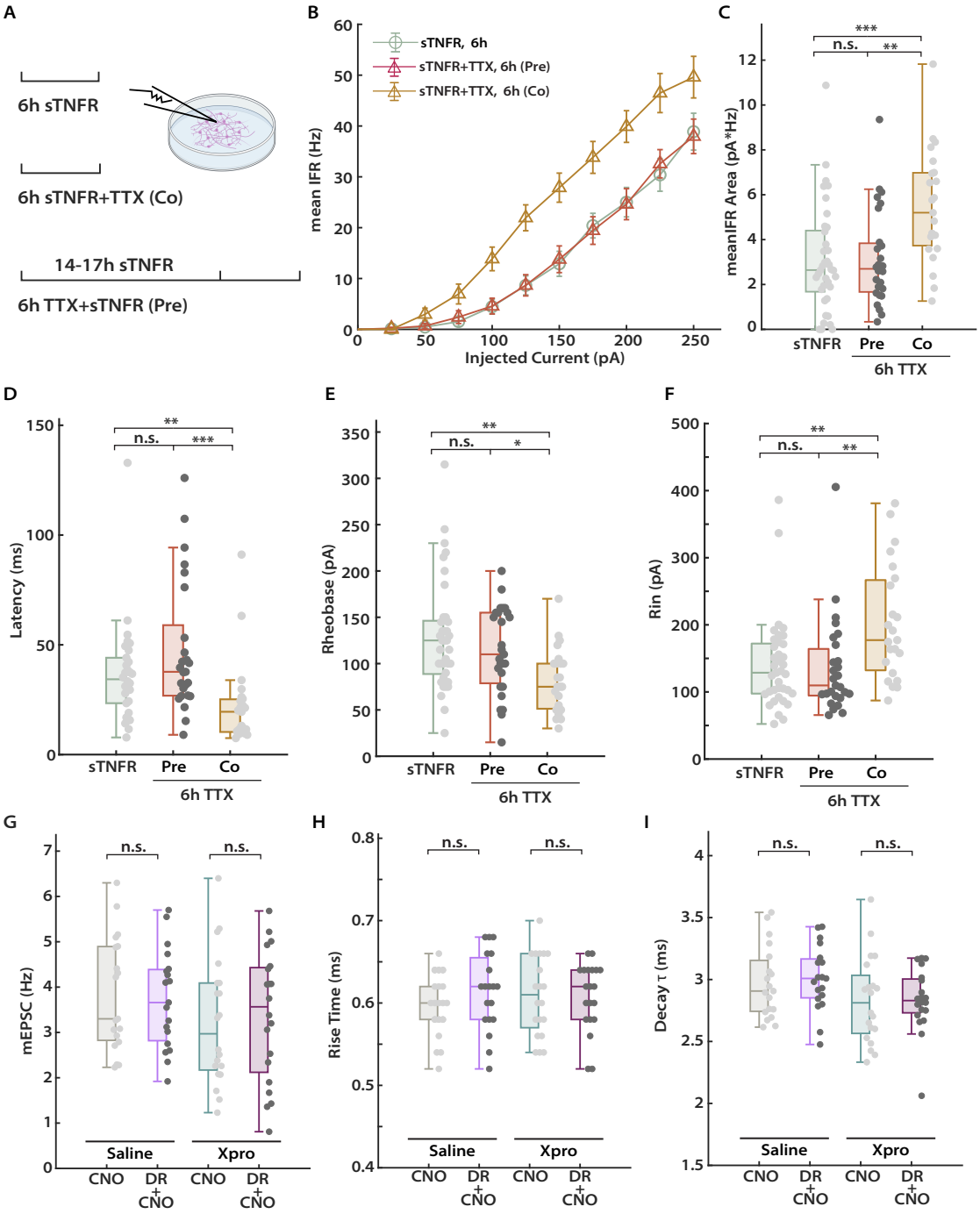
A
6h sTNFR
6h sTNFR+TTX (Co)
14-17h sTNFR
6h TTX+sTNFR (Pre)
B
sTNFR, 6h
sTNFR+TTX, 6h (Pre)
sTNFR+TTX, 6h (Co)
mean IFR (Hz)
Injected Current (pA)
C
meanIFR Area (pA*Hz)
n.s.
**
***
sTNFR
Pre
Co
6h TTX
D
Latency (ms)
E
Rheobase (pA)
F
Rin (pA)
G
mEPSC (Hz)
H
Rise Time (ms)
I
Decay τ (ms)
Saline
Xpro
CNO
DR + CNO

Figure S2. IHP expression *in vitro* requires TNFα signaling. Related to Figure 2.

(A) Experimental paradigm. Cultured neocortical neurons were treated with sTNFR alone, or together with TTX (Co), or pretreated with sTNFR for 14-17 hours before adding TTX (Pre).

(B) Comparison of F-I curves for pyramidal neurons from the indicated conditions in A. sTNFR, n = 37; Pre, n = 27; Co, n = 23.

(C) Comparison of the area under F-I curve for each neuron from the indicated conditions. Kruskal-Wallis test with Tukey post-hoc correction: sTNFR vs. Pre, p = 0.9950; sTNFR vs. Co, p = 7.88E-4; Pre vs. Co, p = 0.0026.

(D) Comparison of latency to the first spike at 175 pA of current injection from the indicated conditions. Kruskal-Wallis test with Tukey post-hoc correction: sTNFR vs. Pre, p = 0.4979; sTNFR vs. Co, p = 0.0030; Pre vs. Co, p = 8.02E-5.

(E) Comparison of rheobase current from the indicated conditions. Kruskal-Wallis test with Tukey post-hoc correction: sTNFR vs. Pre, p = 0.8431; sTNFR vs. Co, p = 0.0024; Pre vs. Co, p = 0.0232.

(F) Comparison of input neuronal resistance from the indicated conditions. Kruskal-Wallis test with Tukey post-hoc correction: sTNFR vs. Pre, p = 0.8610; sTNFR vs. Co, p = 0.0074; Pre vs. Co, p = 0.0030.

(G) Comparison of the mean mEPSC frequency for L2/3 pyramidal neurons from the indicated conditions. Unpaired T test: Saline, CNO vs. DR+CNO, p = 0.8153; Xpro, CNO vs. DR+CNO, p = 0.7763.

(H) Comparison of the mEPSC rise time for L2/3 pyramidal neurons from the indicated conditions. Unpaired T test: Saline, CNO vs. DR+CNO, p = 0.2558; Xpro, CNO vs. DR+CNO, p = 0.9891.

(I) Comparison of the mEPSC decay time constant (τ) for L2/3 pyramidal neurons from the indicated conditions. Unpaired T test: Saline, CNO vs. DR+CNO, p = 0.5019; Xpro, CNO vs. DR+CNO, p = 0.6949.

G through I: same samples sizes as shown in Figures 2C.

Figure S3

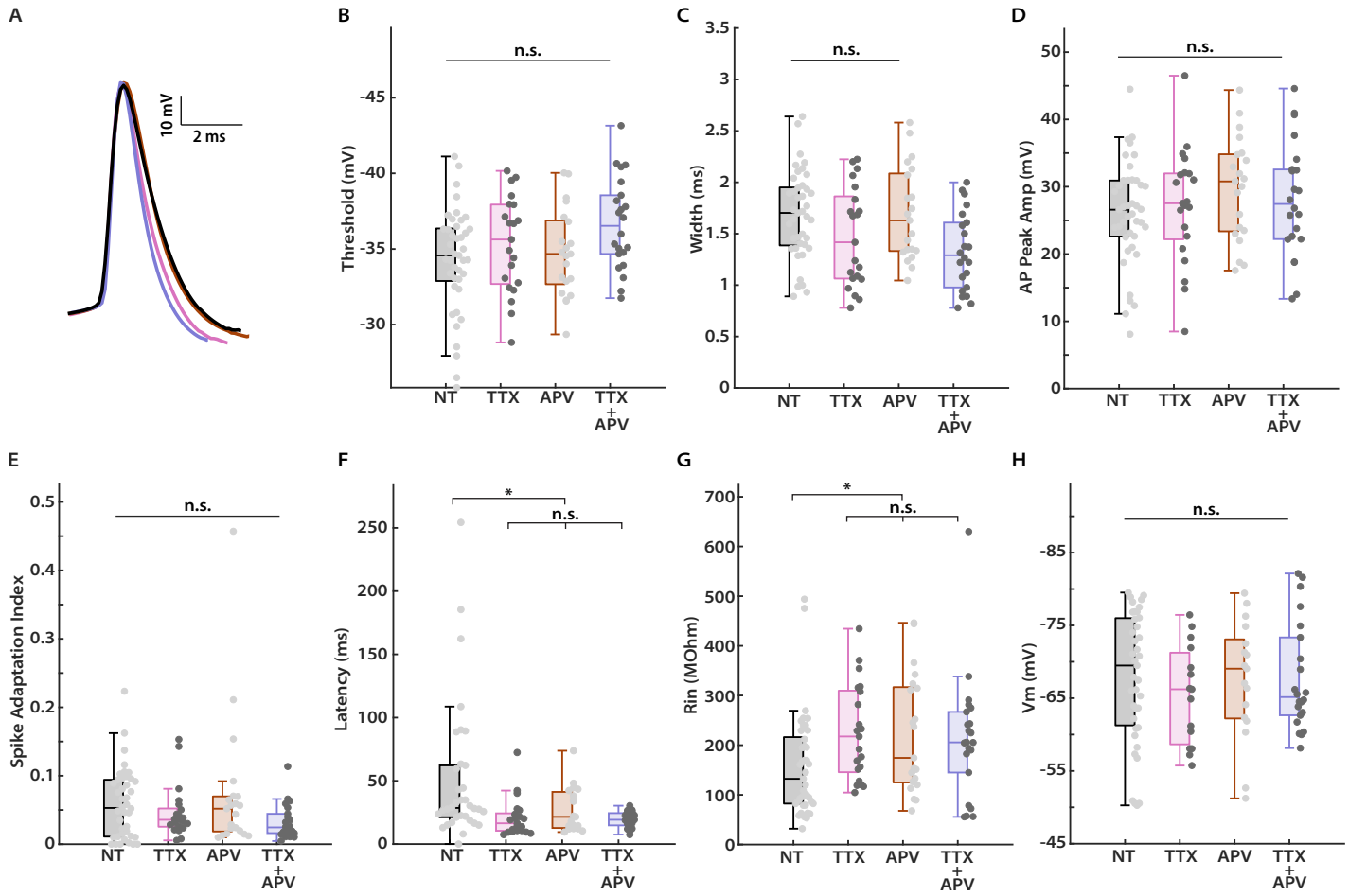
A
10 mV
2 ms
B
Threshold (mV)
n.s.
C
Width (ms)
n.s.
D
AP Peak Amp (mV)
n.s.
E
Spike Adaptation Index
n.s.
F
Latency (ms)
*
n.s.
G
Rin (MOhm)
*
n.s.
H
Vm (mV)
n.s.
NT
TTX
APV
TTX + APV

Figure S3. Cellular properties that underlie IHP expression *in vitro*. Related to Figure 5.

(A) Overlay of peak-scaled average waveforms of first spikes evoked at the rheobase from the indicated conditions (same color code as in Figure 5B)

(B) Comparison of action potential voltage threshold for the first spike at rheobase from the indicated conditions. Kruskal-Wallis test: $p = 0.4597$.

(C) Comparison of full width at half-maximum for the first spike at rheobase from the indicated conditions. One-way ANOVA test with Tukey post-hoc correction: NT vs. TTX, $p = 0.2528$; NT vs. APV, $p = 1.0000$; NT vs. TTX+APV, $p = 0.0122$; TTX vs. APV, $p = 0.3561$; TTX vs. TTX+APV, $p = 0.7067$; APV vs. TTX+APV, $p = 0.0359$.

(D) Comparison of the peak amplitude for the first spike at rheobase from the indicated conditions. One-way ANOVA test: $p = 0.3799$.

(E) Comparison of spike frequency adaptation at 250 pA of current injection from the indicated conditions. Kruskal-Wallis test: $p = 0.0505$.

(F) Comparison of latency to the first spike at 150 pA of current injection from the indicated conditions. Kruskal-Wallis test with Tukey post-hoc correction: NT vs. TTX, $p = 1.00E-3$; NT vs. APV, $p = 0.0796$; NT vs. TTX+APV, $p = 0.0095$; TTX vs. APV, $p = 0.4593$; TTX vs. TTX+APV, $p = 0.9667$; APV vs. TTX+APV, $p = 0.7636$.

(G) Comparison of neuronal input resistance from the indicated conditions. Kruskal-Wallis test with Tukey post-hoc correction: NT vs. TTX, $p = 0.0133$; NT vs. APV, $p = 0.0300$; NT vs. TTX+APV, $p = 0.0599$; TTX vs. APV, $p = 0.9834$; TTX vs. TTX+APV, $p = 0.8958$; APV vs. TTX+APV, $p = 0.9871$.

(H) Comparison of resting membrane potential from the indicated conditions. Kruskal-Wallis test: $p = 0.7093$.

A through H: same sample sizes as shown in Figure 5C.

Figure S4

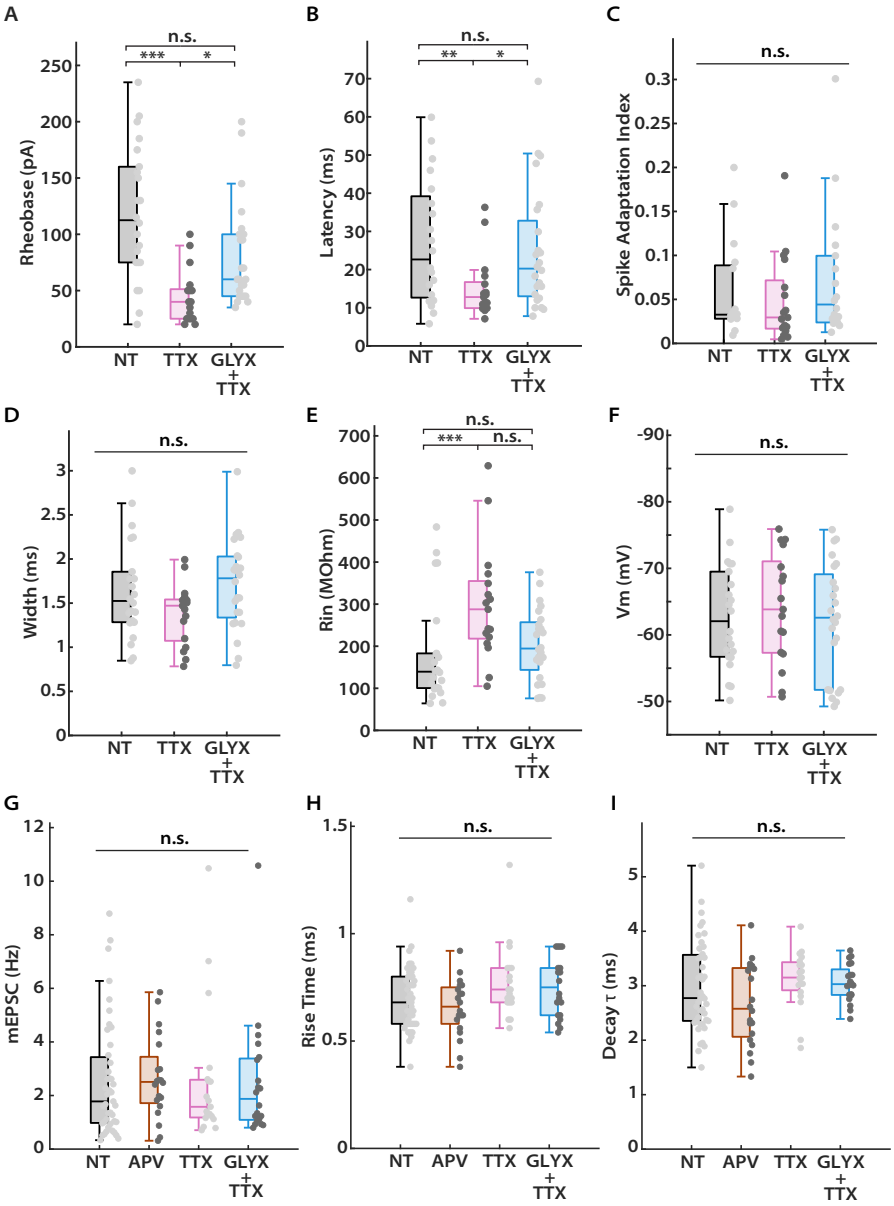
A
Rheobase (pA)
n.s.
***
*
NT
TTX
GLYX + TTX
B
Latency (ms)
n.s.
**
*
C
Spike Adaptation Index
n.s.
D
Width (ms)
n.s.
E
Rin (MOhm)
n.s.
***
n.s.
F
Vm (mV)
n.s.
G
mEPSC (Hz)
n.s.
NT
APV
TTX
GLYX + TTX
H
Rise Time (ms)
n.s.
I
Decay τ (ms)
n.s.

Figure S4. NMDAR positive allosteric modulator GLYX does not affect synaptic and intrinsic cellular properties. Related to Figure 7.

(A) Comparison of rheobase current from the indicated conditions. Kruskal-Wallis test with Tukey post-hoc correction: NT vs. TTX, $p = 2.50E-5$; NT vs. GLYX+TTX, $p = 0.1200$; TTX vs. GLYX+TTX, $p = 0.0187$.

(B) Comparison of latency to the first spike at 200 pA of current injection from the indicated conditions. Kruskal-Wallis test with Tukey post-hoc correction: NT vs. TTX, $p = 0.0097$; NT vs. GLYX+TTX, $p = 0.6686$; TTX vs. GLYX+TTX, $p = 0.0172$.

(C) Comparison of spike frequency adaptation at 200 pA of current injection from the indicated conditions. Kruskal-Wallis test: $p = 0.4271$.

(D) Comparison of full width at half-maximum for the first spike at rheobase from the indicated conditions. One-way ANOVA test: $p = 0.0915$.

(E) Comparison of neuronal input resistance from the indicated conditions. Kruskal-Wallis test with Tukey post-hoc correction: NT vs. TTX, $p = 3.70E-3$; NT vs. GLYX+TTX, $p = 0.4465$; TTX vs. GLYX+TTX, $p = 0.0800$.

(F) Comparison of resting membrane potential from the indicated conditions. One-way ANOVA test: $p = 0.7365$.

(G) Comparison of the mean mEPSC frequency from the indicated conditions. One-way ANOVA test: $p = 0.7161$.

(H) Comparison of the mEPSC rise time from the indicated conditions. One-way ANOVA test: $p = 0.0845$.

(I) Comparison of the mEPSC decay time constant (τ) from the indicated conditions. One-way ANOVA test: $p = 0.1580$.

A through F: same sample sizes as shown in Figure 7B.

G through I: same sample sizes as shown in Figure 7E.

Figure S5

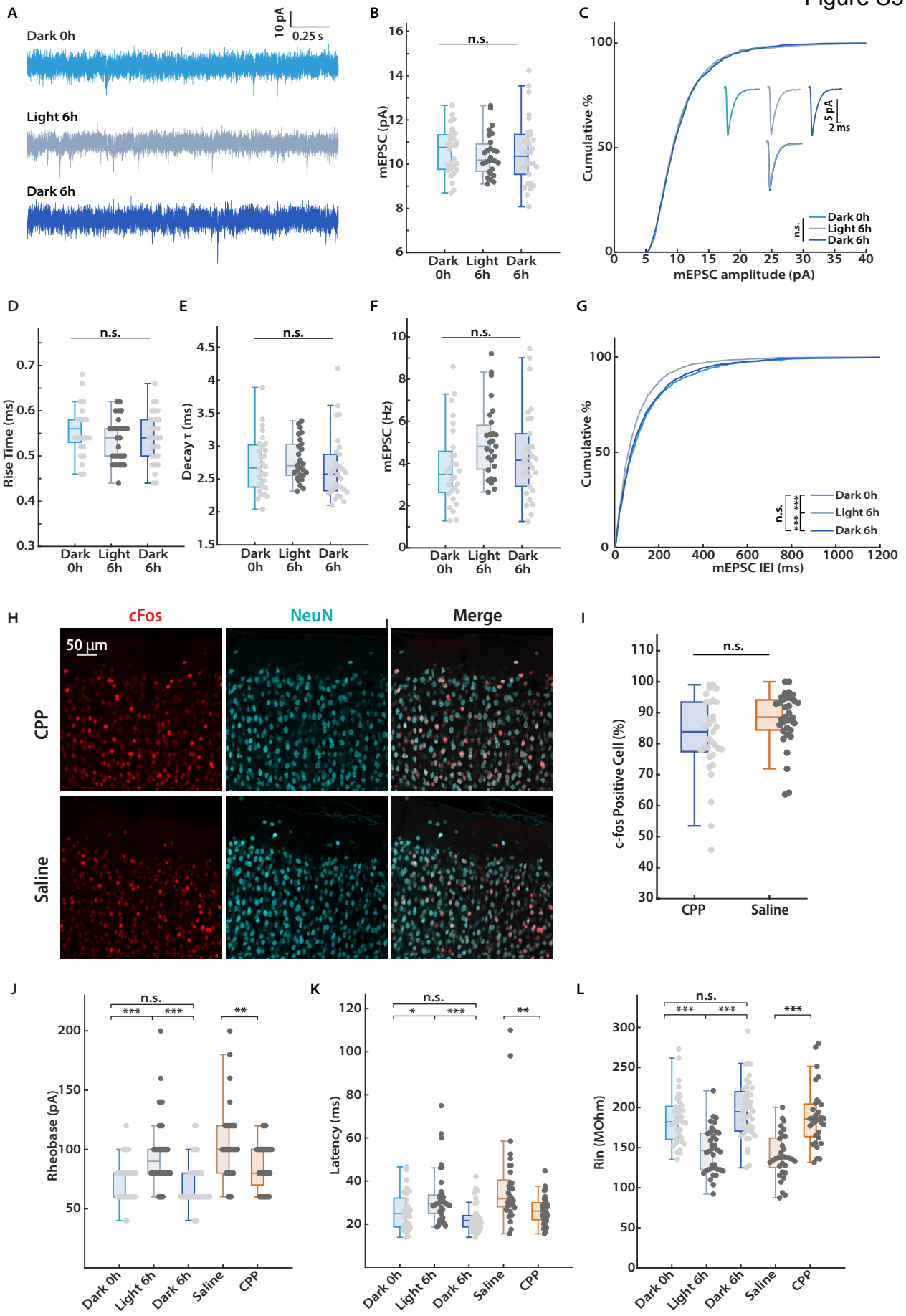
A
Dark 0h
Light 6h
Dark 6h
10 pA
0.25 s
B
n.s.
mEPSC (pA)
Dark 0h
Light 6h
Dark 6h
C
Cumulative %
mEPSC amplitude (pA)
5 pA
2 ms
n.s.
Dark 0h
Light 6h
Dark 6h
D
n.s.
Rise Time (ms)
E
n.s.
Decay τ (ms)
F
n.s.
mEPSC (Hz)
G
Cumulative %
mEPSC IEI (ms)
n.s.
***
***
Dark 0h
Light 6h
Dark 6h
H
cFos
NeuN
Merge
50 µm
CPP
Saline
I
n.s.
c-fos Positive Cell (%)
CPP
Saline
J
n.s.
***
***
**
Rheobase (pA)
Dark 0h
Light 6h
Dark 6h
Saline
CPP
K
n.s.
*
***
**
Latency (ms)
Dark 0h
Light 6h
Dark 6h
Saline
CPP
L
n.s.
***
***
***
Rin (MOhm)
Dark 0h
Light 6h
Dark 6h
Saline
CPP

Figure S5. Light-driven increase in correlation leads to downregulation of intrinsic excitability without affecting synaptic strength in freely behaving animals. Related to Figure 8.

(A) Representative traces of mEPSC recordings in L2/3 pyramidal neurons from the three indicated timepoints in Figure 8E.

(B) Comparison of the mean mEPSC amplitude for L2/3 pyramidal neurons from the three indicated timepoints. Dark 0h, n = 28, 3 animals; Light 6h, n = 27, 3 animals; Dark 6h, n = 30, 3 animals. One-way ANOVA test: p = 0.8820.

(C) Cumulative distribution of mEPSC amplitudes from the three indicated timepoints. Inset: Upper, unscaled average waveforms from the three timepoints, respectively; Lower, overlay of all three waveforms. Kolmogorov-Smirnov test: Dark 0h vs. Light 6h, p = 0.4914; Dark 0h vs. Dark 6h, p = 0.1730; Light 6h vs. Dark 6h, p = 0.3544.

(D) Comparison of the mEPSC rise time from the three indicated timepoints. One-way ANOVA test: p = 0.3937.

(E) Comparison of the mEPSC decay time constant (τ) from the three indicated timepoints. One-way ANOVA test: p = 0.2019.

(F) Comparison of the mean mEPSC frequency from the three indicated timepoints. One-way ANOVA test: p = 0.0700.

(G) Cumulative distribution of inter-event intervals (IEIs) from the three indicated timepoints. Kolmogorov-Smirnov test: Dark 0h vs. Light 6h, p = 1.14E-12; Dark 0h vs. Dark 6h, p = 0.1358; Light 6h vs. Dark 6h, p = 1.27E-8.

(H) Representative images of cFos expression in the L2/3 of mouse V1 following acute CPP (upper row) and saline (lower row) injections, respectively.

(I) Quantification and comparison of the percentage of cFos-positive neurons (out of all NeuN-positive neurons) following CPP and saline injections. Each data point indicates the cFos positive rate calculated from a region of interest in L2/3 selected from a sectioned V1-containing slice. CPP, n = 33, 3 animals; Saline, n = 34, 3 animals. Mann-Whitney U test, p = 0.0770.

(J) Comparison of rheobase current from the indicated conditions. Left three groups, Kruskal-Wallis test with Tukey post-hoc correction: Dark 0h vs. Light 6h, p = 6.02E-6; Dark 0h vs. Dark 6h, p = 0.5397; Light 6h vs. Dark 6h, p = 3.27E-6; Right two groups, Mann-Whitney U test: CPP vs. Saline, p = 0.0049.

(K) Comparison of latency to the first spike at 200 pA of current injection from the indicated conditions. Left three groups, Kruskal-Wallis test with Tukey post-hoc correction: Dark 0h vs. Light 6h, p = 0.0321; Dark 0h vs. Dark 6h, p = 0.2790; Light 6h vs. Dark 6h, p = 1.15E-4; Right two groups, Mann-Whitney U test: CPP vs. Saline, p = 0.0029.

(L) Comparison of neuronal input resistance from the indicated conditions. Left three groups, One-way ANOVA test with Tukey post-hoc correction: Dark 0h vs. Light 6h, p = 1.80E-6; Dark 0h vs. Dark 6h, p = 0.3679; Light 6h vs. Dark 6h, p = 1.63E-9; Right two groups, unpaired T test: CPP vs. Saline, p = 3.43E-7.

J through L: same sample sizes as shown in Figures 8F and 8J.